THE SMITH CLOUD: A CASE STUDY OF THE DYNAMIC DISRUPTION OF A HIGH-VELOCITY GAS CLOUD ON APPROACH TO THE MILKY WAY GALAXY

by

JOHANNA T. VAZQUEZ

Baccalaureate of Science, 2020
Randolph College
Lynchburg, VA

Associate of Arts & Sciences, 2017
Central Virginia Community College
Lynchburg, VA

Submitted to the Graduate Faculty of the
College of Science and Engineering
Texas Christian University
in partial fulfillment of the requirements
for the degree of

Master of Science

December 2022

THE SMITH CLOUD: A CASE STUDY OF THE DYNAMIC DISRUPTION OF A HIGH-VELOCITY GAS CLOUD ON APPROACH TO THE MILKY WAY GALAXY
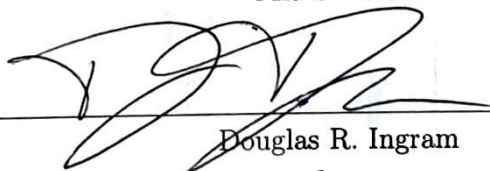
by

Johanna T. Vazquez

Dissertation Approved:

_____
Kathleen A. Barger

_____
Peter M. Frinchaboy III

_____
Mia S. Bovill

_____
Douglas R. Ingram

_____
For The College of Science and Engineering

Contents

List of Figures

List of Tables

List of Abbreviations

Abbreviation	Meaning
T_B	Brightness Temperature (K)
ℓ	Galactic longitude (degrees)
b	Galactic Latitude (degrees) or Doppler parameter $(\mathrm{km\,s^{-1}})$
n_{H}	Number density of hydrogen (atoms $\mathrm{cm^{-3}}$)
n_γ	Number density of ionizing photons of hydrogen (photons $\mathrm{cm^{-3}}$)
$N_{X(n)}$	Column density of element X with ionization n (atoms $\mathrm{cm^{-2}}$)
U	n_γ/n_{H}, where n_γ is the number density of ionizing photons. This quantity is also known as the ionization parameter.
IC(X)	Ionization Correction of Element X
L_*	Cutoff point of the Schechter function that describes the number of galaxies with different luminosities. Both the Milky Way and Andromeda galaxies are roughly 1 L_*.
HST	Hubble Space Telescope
COS	Cosmic Origins Spectrograph on the Hubble Space Telescope
LSR	Local Standard of Rest
HVC	High-Velocity Cloud
GBT	Green Bank Telescope
ISM	Interstellar Medium
IGM	Intergalactic Medium
MW	Milky Way
SC	Smith Cloud
AOD	Apparent Optical Depth
H I	read as "H one," meaning neutral hydrogen
S II	read as "sulfur two," meaning singly-ionized sulfur.
Si III	read as "silicon three," meaning doubly-ionized silicon

Chapter 1

Introduction

1.1 The Fuel for Stars

In order to form new stars and planets, gas must be dense enough and cold enough to gravitationally collapse in on itself and resist the opposing collisional pressure. Although conditions in the past were suitable to for the creation of new stars, it is possible that as many as 95% of the stars that will ever exist have already been born (Sobral et al. 2013). This is due to a multitude of factors, mostly the gas and so-called "metals" (elements heavier than helium) being locked away inside the M and K-Type Main Sequence Stars that will live longer than the current age of the Universe.

The avenues of star-formation in the modern Universe are still largely unsolved; however, metal-rich gas is a crucial component of star-formation (Choi & Nagamine 2009). Despite the Milky Way galaxy having $M \sim 10^9 M_\odot$ of gas in its disk, its star formation rate is only $\dot{M}_{\mathrm{SFR}} = 1 - 3 M_\odot \ \mathrm{yr}^{-1}$ (Putman et al. 2012; Smith et al. 1978; Robitaille

& Whitney 2010). Since the gas reservoirs of galaxies in the modern Universe are being ever-depleted, external sources of metal-rich gas are needed for galaxies to continue their current rates of star-formation. One such avenue for the accretion of this new gas is in the form of high-velocity clouds.

1.1.1   High-Velocity Clouds

Gas is constantly flowing in and out of galaxies like our Milky Way (MW; eg: Barger et al. 2020, Fox et al. 2019, Lockman et al. 2008). Among these gas clouds flowing into and out of our galaxy, there are intermediate-velocity clouds (IVCs), with Local Standard-of-Rest velocities of 50 km s^{-1} $\lesssim |v_{\mathrm{LSR}}| \lesssim$ 100 km s^{-1} and high-velocity clouds (HVCs) with $|v_{\mathrm{LSR}}| \gtrsim$ 100 km s^{-1} (see Figure 1.1). When galaxies run out of fuel to form new stars, HVCs may provide an important avenue for continued star formation (Lépine et al. 1999). HVCs may also have a wide variety of origins. One such origin possibility is the intergalactic medium (IGM): the primordial gas left over from cosmological structure formation (Madau 2002). Another avenue to form an HVC is from stellar feedback from the Milky Way. More specifically, high star-forming regions or supernovae may have kicked material out of our Galaxy's plane. This material may be better suited to star-formation, as it is likely to have more metals and more avenues to cool and condense .

Although high metallicity gas has great potential to form stars in the future, it must first make its way to a galaxy's plane before it can begin to condense and form stars and planets (Shu & Adams 1987; Kennicutt & Evans 2012; Schinnerer et al. 2013; Putman

et al. 2012). In order to do so, it must cross through the Galactic halo, a shell of hot $(T \sim 10^6$ K) gas surrounding the Galactic plane (Kerp et al. 1999; Putman et al. 2012). Understanding the survivability of this gas is paramount to extrapolating the ability of these HVCs to form new stars and planets. The Smith Cloud is a very strong candidate to study how gas clouds are affected by ram-pressure stripping and the ionizing radiation from the Milky Way galaxy. This is because many of the physical properties of the Smith Cloud are well-constrained (Hill et al. 2009; Hill et al. 2013; Fox et al. 2016).
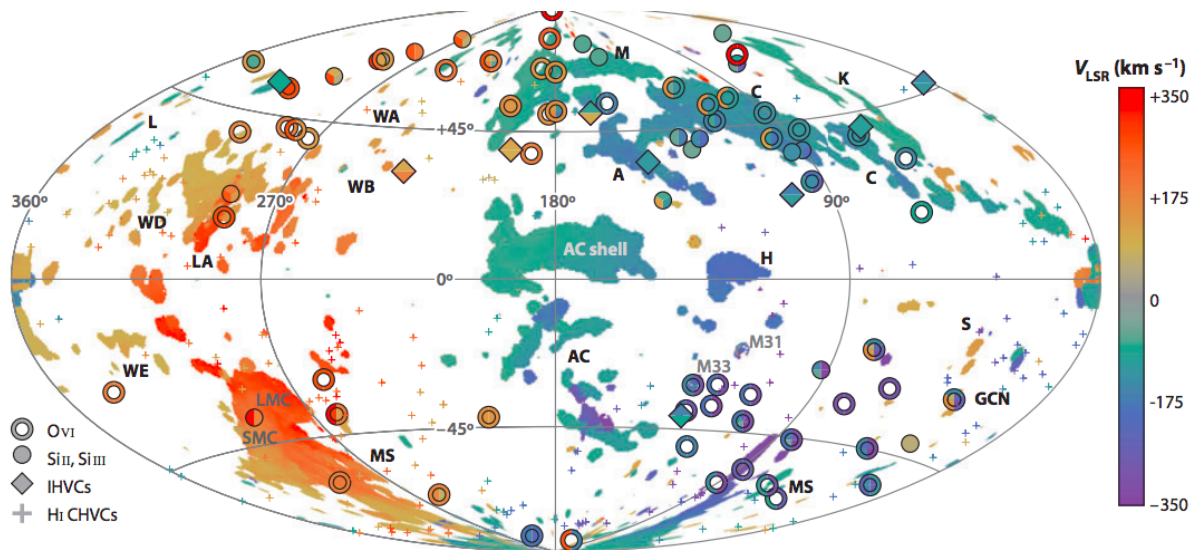
Figure 1.1: A map created by Kalberla & Kerp (2009), using the Leiden-Argentine-Bonn (LAB) Neutral Hydrogen Survey, detailing the distribution of neutral hydrogen (or H I around the Milky Way galaxy in galactic coordinates. Here, H I gas from the Milky Way has been subtracted out. Gas is color-coded by its local standard of rest (LSR) velocity along the line of sight and shape-coded based on detected ions of O VI, Si II, III, whether or not the cloud is an intermediate-high-velocity cloud (IHVC), and whether the cloud is an H I-compact HVC (CHVC; Putman et al. 2012). The "S" label represents the Smith Cloud at $(\ell, b, v_{\mathrm{LSR}}) \approx (+42.0°, -24.2°, +75\mathrm{km\ s}^{-1})$, the object of this thesis.

1.2 The Smith Cloud

In order to provide new gas for the Milky Way (MW) galaxy, the Smith Cloud will need to survive its journey through the MW's galactic halo. This 10^6 K gas surrounding the MW is a large impediment to any gas clouds that may deposit onto our Galaxy. The Smith Cloud has been vigorously studied since its discovery by Gail Smith (1963). Much of the Smith Cloud's properties have been well-constrained, such as its prograde orbit (Lockman et al. 2008), its magnetic field (Hill et al. 2013), and metallicity (Fox et al. 2016) in the trailing wake. However, the adjacent cloud fragments have not yet been studied with absorption-line spectroscopy or photoionization simulations. Understanding regions closer to the main body of the Smith Cloud in addition to the trailing wake could provide useful information for how this HVC is being disrupted and mixed by the Galactic halo.

To close this gap in the field's knowledge, we have used the cumulative sightlines from both Fox et al. (2016) and two new sightlines observed with the Hubble Space Telescope (HST), Green Bank Telescope (GBT), and Galactic All-Sky Survey (GASS; Kalberla et al. 2010). We use absorption-line and emission-line fitting techniques to obtain a gradient of ionization parameters, such as density, temperature, pressure, and ionization fraction in different regions of the Smith Cloud.

1.2.1 Origins

Despite the Smith Cloud being one of the most well-understood HVCs, its origins are still not fully constrained, although it seems to have originated from the Milky Way (Tepper-García & Bland-Hawthorn 2018; Fox et al. 2016; Henley et al. 2017). Fox et al. (2016)
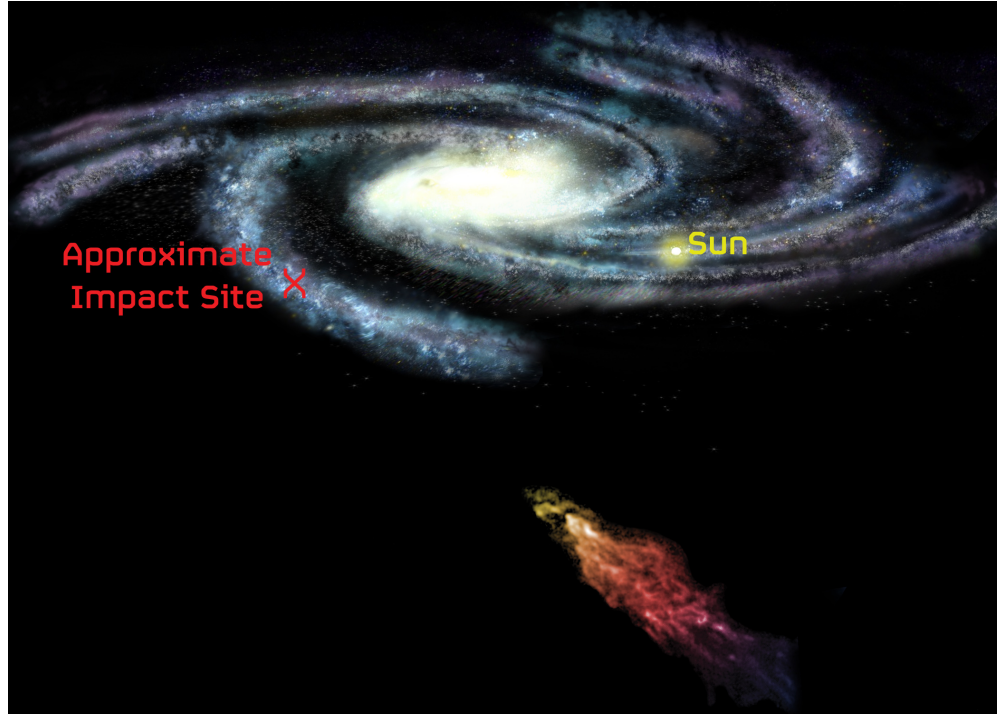
Figure 1.2: Cartoon describing the proposed future trajectory of the Smith Cloud, which includes a collision with the Milky Way's Galactic plane (credit: Bill Saxton/National Radio Astronomy Observatory).

first explored the origin question with a combined radio and UV study of three sightlines along the tail of the Smith Cloud. They found the metallicity of the Smith Cloud to be $Z = -0.28 \pm 0.14$ in log scale, which corresponds to $Z = 0.53^{+0.21}_{-0.15} Z_\odot$. We may not expect material from the Milky Way's galactic halo to have this high of a metallicity, which could imply an origin from the Milky Way galaxy. Since then, some, such as Marasco & Fraternali (2016) have explored the possibility of a galactic fountain kicking the SC out of the MW, However, argument persists as to the true origins. Some, like Tepper-García & Bland-Hawthorn (2018), argue that the Smith Cloud could have originated from a gas cloud or small galaxy colliding with the Milky Way's disk in the past. The analysis of these two additional sightlines could prove useful for further constraining the origin of the Smith Cloud.

1.2.2 Locations

Two of the sightlines —UVQSJ203335.89-032038.5 (shortened hereafter to Sightline A) & UVQSJ204402.02-07810.0 (Sightline B) —trace an offshoot fragment of the cloud. The other three sightlines —RXJ2043.1+0324 (Sightline C), PG2112+059 (Sightline D), and RXJ2139.7+0246 (Sightline E) —trace the trailing wake of the Smith Cloud. As the Smith Cloud travels through this apparent wind, it is shaped into a comet-like structure, with a compact head (upper right in Figure 2.1) and diffuse tail (lower left in Figure 2.1; Fox et al. 2016).

Obtaining a grid of ionization conditions in different regions of the Smith Cloud would provide great insight into how the cloud is being disrupted by and mixing with the surrounding galactic halo. This grid of physical parameters could also provide a useful resource to the HVC simulation community to investigate the survivability of infalling HVCs.

Along with understanding these ionization conditions, such as density, temperature, and pressure, the metallicity of these two new sightlines can also shed light on the origins of the Smith Cloud and how its gas mixes with the Galactic halo. Fox et al. (2016) first explored the metallicity along the tail, which showed a relatively high metallicity nearer to the main body with a lower metallicity further away from the main body.

1.3 Scientific Questions

This thesis aims to answer the following scientific questions:

1. What are the limits of the metallicity, density, pressure, temperature, and ionization within the Smith Cloud?

2. Are these limits different closer to the main body than they are further downstream?

This thesis answers these questions by utilizing H I observations from the Robert C. Byrd Green Bank Telescope (GBT) and Parkes Radio Telescope Galactic All-Sky Survey (GASS; Kalberla et al. 2010; McClure-Griffiths et al. 2009) in parallel with UV observations from the G130M grating on the Cosmic Origins Spectrograph (COS) on the Hubble Space Telescope (HST). We also utilize *Cloudy* c17.01 (Ferland et al. 2017) simulations to derive these limits on the physical parameters in the trailing wake of the Smith Cloud and an adjacent cloud fragment.

Chapter 2

Observational Data & Analysis of

Observations

2.1 Data

To decipher how the ionization properties of the Smith Cloud vary as a function of the distance from the head of the Cloud, we combined radio emission and UV absorption-line observations to investigate the neutral hydrogen and heavy elements, respectively. To explore the distribution of H I in the Smith Cloud, we use radio data from the GBT and GASS/LAB Surveys (Kalberla et al. 2010; McClure-Griffiths et al. 2009). Additionally, we used the Cosmic Origins Spectrograph (COS) on HST to observe heavier elements (or "metals") in multiple ionization states through their far-ultraviolet absorption.

2.1.1 HST Observations

We used the COS instrument to collect light over the 1130Å$\le \lambda \le$ 1440Åwavelength range. Our dataset has a break at 1205Å to 1220Å that is associated with the Lyman α line. These observations span five sightlines along the Smith Cloud (see Figure 2.1) and probe both the trailing wake of this HVC and and clouds that have appear to have fragmented off its main body.

The reduction of these observations consisted of flux calibrating, aligning, and co-adding individual exposures. For the HST/COS observations, we have two versions of this reduction: one that includes all parts of all exposures and another that only includes the time-tagged "night" portion of the exposure during HST crossing through Earth's shadow. We performed this "night-only" reduction to avoid air-glow emission that is produced by molecules in Earth's upper atmosphere that are excited by sunlight. This is a crucial step to take, since this air-glow emission overlaps with two important absorption lines: a neutral oxygen line at $\lambda = 1302$ Å, and a singly-ionized silicon line at $\lambda = 1304$ Å.

ID	Target	Location	$\ell(°)$	$b(°)$	z	FUV (mag)
A	UVQSJ203335.89-0320385	Fragment	42.0	-24.2	0.696	17.74
B	UVQSJ204402.03-0758105	Fragment	38.8	-28.6	0.103	17.78
C	RXJ2043.1+0324	Trailing	49.72	-22.88	0.271	17.29
D	PG2112+059	Trailing	57.04	-28.01	0.457	17.05
E	RXJ2139.7+0246	Trailing	58.09	-35.01	0.260	16.79

Table 2.1: A table of QSO sightline names and the shortened names that we refer to in this study. Here ℓ represents Galactic longitude, b represents Galactic latitude, z represents redshift of the target, and FUV magnitude is the magnitude of the far ultraviolet light of the background QSO.

These observations cover the transitions of multiple low-ionization (i.e, singly ionized) species and a few highly-ionized (i.e., triply ionized) species. These transitions include
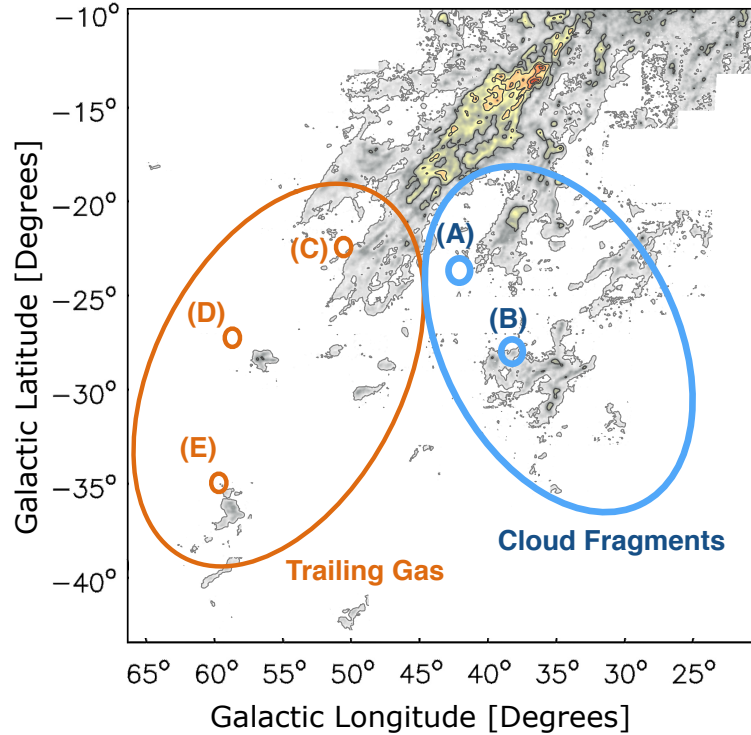
Figure 2.1: The Smith Cloud in H I from Lockman et al. (2008). The colored in areas represent the H I 21-cm column densities. The areas encircled in blue are offshoot fragments of the Smith Cloud that are "above" the main body of the SC with respect to the gravitational potential of the Milky Way. The area encircled in orange is the diffuse tail of the SC that is presumably created by ram-pressure stripping that results from drag as an apparent wind grazes the surface of the SC as it travels through the MW's halo.

Fe IIλ1144, Si IIλ1190, 1193, 1260, 1304, Si IIIλ1206, Si IVλ1393, 1402, S IIλ1250, 1253, 1259, C IIλ1334, and C II$^*\lambda$1335 lines; here, Roman numeral I corresponds to lines associated with neutral elements and each higher integer value indicates a higher ionization state. This list of accessible transitions does not include the neutral hydrogen Lyman lines as the Smith Cloud's absorption is too blended with the Milky Way to recover.

Additionally, we converted the UV spectra first to heliocentric velocity with the low-

redshift relation:

$$v_{\text{helio}} = c \left(\frac{\lambda - \lambda_0}{\lambda_0} \right),$$ (2.1)

where λ represents the wavelength array, λ_0 the central laboratory rest-frame wavelength of the ionic transition we wish to study, and c the speed of light. Further, our spectroscopic observations have already been corrected for Earth's motion, so we did not have to include a conversion from the geocentric to heliocentric reference frames in this process. Additionally, to match the velocity frame of the radio data, we convert to the *kinematic* local standard of rest (LSR) velocity frame with the following relation defined by Meeks (1976):

$$v_{\text{LSR}} = v_{\text{helio}} + v_{\text{apex}} \left[\sin(b) \sin(b_{\text{apex}}) + \cos(b) \cos(b_{\text{apex}}) \cos(\ell - \ell_{\text{apex}}) \right],$$ (2.2)

where $v_{\text{apex}} = +20$ km/s refers to the radial velocity of the local standard of rest, $b_{\text{apex}} = 23.5°$ is the Galactic latitude of the local standard of rest, and $\ell_{\text{apex}} = 55.9°$ is the Galactic longitude of the local standard of rest (Francis & Anderson 2014; Francis & Anderson 2009). Both the heliocentric and local standard of rest frames are in the frame that corresponds to the Sun, but the heliocentric frame accounts for the actual motion of the Sun and the local standard of rest frame represents and idealized orbit of the Sun around the Milky Way's galactic center.

2.1.2 Radio Observations

We used H I 21-cm emission-line observations along all five sightlines with the GBT from Lockman et al. (2008) and the kinematically integrated H I maps from that study (see Figure 2.1). These pointed observations along our sightlines have a sensitivity of $\log{(N_{\text{H I}})} = 18.18$. We use these observations to quantify the H I column densities. We also used kinematically resolved archival observations of this same emission line that were taken with the Parkes Radio Telescope, which enabled us to explore and compare the kinematic structure of H I clouds near our sightlines.

2.2 Analysis of Observations

2.2.1 Line Fitting

We measured the column densities, line centers, and line widths of various ionic transitions by fitting the emission- and absorption- lines with Gaussian and Voigt line profiles, respectively. This information provides insight on the kinematics of the Smith Cloud as well as its composition.

2.2.2 Absorption Lines

We used Voigt line profiles to fit our absorption lines as they account for the contributions that are associated with natural line broadening that is Lorentzian in shape, thermal broadening that is Gaussian in shape, and collisional broadening that is Lorentzian in shape. A Voigt line profile is the result of the convolution of a Gaussian and Lorentzian

profile. The Gaussian profile specifically models the line-of-sight component of velocity from thermal motion. This profile has a deviation parameter σ, which is the standard deviation from the mean wavelength due to these Doppler shifts (Draine 2011). The Lorentzian profile associated with natural broadening is due to the Heisenberg Uncertainty Principle, which states that there is an inherent uncertainty in the discrete energies of transitions (Draine 2011). This probability distribution also arises as a result of collisions within a gas cloud (Draine 2011). Note that the internal collisions generally have a greater effect on the shape of the profile than natural broadening (Draine 2011). This profile has a deviation parameter Γ, which, in this probability density function, the probability of falling within the range $\lambda \in [\lambda_0 - \Gamma, \lambda_0 + \Gamma]$ (where x_0 is the mean) is exactly one-half. We fit our absorption spectra with the VoigtFit Python package (Krogager 2018). This program also calculates the column densities, velocity centers, and line widths of the absorbers that would result in the observed line strengths using oscillator strengths, damping parameters, and rest wavelengths of each transition.

Primarily, in this study, we focus on the S II, Si II, Si III. We use the S II line to trace the metallicity of the cloud. We use this line to trace metallicity, as sulfur does not significantly deplete onto dust grains in the warm-ionized medium, the type of gas found in the Smith Cloud (Jenkins 2009; Draine 2011). We then use take the ratio of (1) the relative column density ratio of $N_{\text{S II}}/N_{\text{H I}}$ and (2) the S/H gas-phase abundance ratio found in the Sun to obtain

$$[\text{S II/H I}] \equiv \log_{10}\left(\frac{N_{\text{S II}}}{N_{\text{H I}}}\right)_{\text{SC}} - \log_{10}\left(\frac{\text{S}}{\text{H}}\right)_{\odot} \tag{2.3}$$

We are additionally interested in the silicon lines since silicon is the only element with viable absorption lines with consecutive ionization species within the wavelengths we observe with HST/COS. Therefore, we use an ionization ratio of Si III/Si II in photoionization simulations (discussed in Chapter 3) to provide a standard measure for the ionization conditions within the Smith Cloud. Although Si IV has two absorption lines within the wavelength range of our spectrum, we have to consider that Si IV and Si III may probe two different regimes of the Smith Cloud. Si III likely traces the inner, more cooler region along the line of sight, whereas Si IV is more likely to probe highly ionized gas on the shell of the Smith Cloud that is being directly photoionized by the Milky Way.

2.2.3 Apparent Optical Depth (AOD)

Some of our absorption lines are saturated. This saturation occurs when there is too much intervening material between the observer and the background QSO, causing 100% of the background light to be absorbed in a certain color range (see Figure 2.2). This means that there are more absorbing particles than are predicted by the area of the absorption feature. Further, these saturated lines have flat bottoms that are not described by a Voigt line profile. This means that we are unable to determine the actual column density of the absorbing material and can only provide a lower limit. We determine this lower limit using the apparent optical depth (AOD) method that was developed by Savage & Sembach (1991).

For saturated lines, we determine a lower bound on the column density using information about the normalized flux area of the transition species the following AOD method
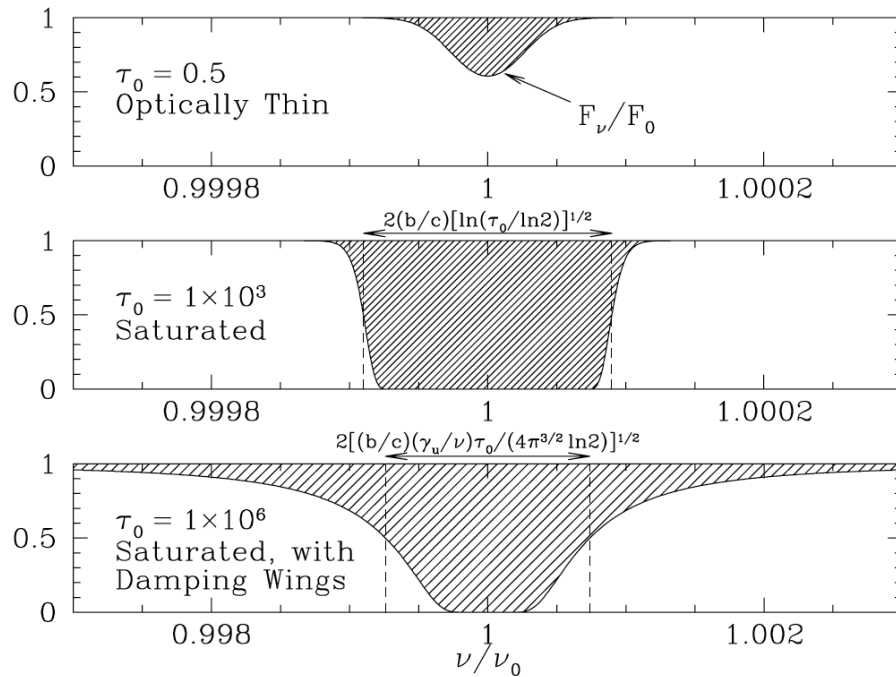
Figure 2.2: Figure from Draine (2011) detailing three possibilities for an absorption line. On the top panel is an optically thin absorption line, which means the entire profile is visible to us. On the middle panel is a saturated absorption profile, meaning for colors close to ν_0, all of the background light is blocked by intervening material absorbing at those frequencies. The bottom panel is a saturated profile with damping wings.

relationship:

$$N_X > \frac{m_e c}{\pi e^2 f_X \lambda_X} \int_{v_{\min}}^{v_{\max}} \ln\left(\frac{F_{\text{continuum}}(v)}{F_{\text{observed}}(v)}\right) dv. \tag{2.4}$$

where N_X, f_X, λ_X represent the column density, oscillator strength, and central wavelength of an ionic species X, respectively. The constants m_e, c, and e respectively represent the electronic mass, speed of light, and elementary charge constants. For optically thin profiles (see Figure 2.2), this method would yield an accurate estimation on the column density. However, because the MW and SC can be kinematically confused around $v_{\text{LSR}} \approx +60$ km s^{-1}, the integrated velocity range needs a hard limit near this $+60$ km s^{-1}. For both new sightlines (A and B), we compare the saturated line to a line that is fitted well. For Sightline A, this line is Si IIλ1190. For Sightline B, this line is C II*λ1335. We use the v_0 and b values extracted from the Voigt fits of these lines to provide the lower column density bound for saturated lines (See Figure 2.2 for visualization of saturated lines). For the so-called High-Confidence Line on each sightline, we take the velocity bounds to be $v_0 - b/2 \leq v_t \leq v_0 + 2b$. Here, v_t is the variable velocity of the transition, v_0 is the center velocity of a high-confidence line, and b is the Doppler parameter. We use this AOD method on the Si III line on Sightlines A and B, as this line is completely saturated and blended with the Milky Way (see Figures 2.7, 2.8).

2.2.4   Radio Analysis

To determine the H I column density, we integrated the provided **brightness temperature** spectra and converted this area under the brightness temperature curve to column

density using the following relationship from Dickey & Lockman (1990):

$$N_{\text{H I}} = 1.823 \times 10^{18} \, \frac{\text{atoms}}{\text{cm}^2} \int_{v_{\text{min}}}^{v_{\text{max}}} \frac{T_B(v)dv}{\text{K}},$$

(2.5)

which assumes that the cloud is transparent to 21-cm light such that all the emission from the cloud is able to escape. Here, the brightness temperature represents how much light we received per velocity bin from the sightline and is proportional to its intensity. To get errorbars on the H I column density on GBT, we first take a splice of noise in the spectrum and find the root-mean-square of the brightness temperature as σ_T. To determine the error in the $N_{\text{H I}}$ measurement, we use the following relation from Wolfe et al. (2016):

$$\sigma_{N_{\text{H I}}} = 1.8223 \times 10^{18} \left(\frac{\sigma_T}{\text{K}} \right) \left(\frac{\sqrt{v_{\text{FWHM}} \, \Delta v}}{\text{km/s}} \right) \text{cm}^{-2}.$$

(2.6)

If we use a characteristic $\sigma_T = 6\text{mK}$, FWHM of 25 km/s, and a velocity bin of 0.8 km/s, we find a sensitivity of $\log N_{\text{H I}} = 17.7$ and a 3σ detecton limit of 18.18. Since we report $N_{\text{H I}}$ logarithmically, we derive the relation for the logarithmic error according to Taylor (1997):

$$\sigma_{\log_{10} N_{\text{H I}}} = \frac{\partial \log_{10} N_{\text{H I}}}{\partial N_{\text{H I}}} \sigma_{N_{\text{H I}}} = \frac{\sigma_{N_{\text{H I}}}}{N_{\text{H I}} \ln 10}$$

(2.7)

2.3 Results

We successfully fit the neutral hydrogen lines as well as some metal absorption lines along the new sightlines A and B. The other previous sightlines (C, D, and E) were previously fit by Fox et al. (2016). For those sightlines, we provide a lower estimate using the AOD

method discussed in the previous section. As discussed in the last section, some lines were too saturated and blended to consider the VoigtFit outputs.

2.3.1 UVQSJ203335 (Sightline A)

If we look at the plot stack (see Figure 2.7), we can see that the center velocity of the intermediate-velocity cloud (IVC) H I component does not match well with the UV absorption. The mean velocity of the IVC H I is $v_{\mathrm{LSR}} \approx +45$ km s^{-1}; whereas the mean velocity of the UV absorption is $v_{\mathrm{LSR}} \approx +110$ km s^{-1}. In order to convince ourselves that this UV absorption is indeed part of the Smith Cloud, we use data from the Galactic All-Sky Survey (GASS) (Kalberla et al. 2010; McClure-Griffiths et al. 2009). Using this data, we explored the column density and kinematic properties of the high-velocity H I near our sightline.

To first ensure that this UV absorption is part of the Smith Cloud, we must observe the nearby high-velocity H I to ensure it is morphologically consistent with the Smith Cloud. In order to perform this, we use a **Moment 0 map**. This is a map of numerically-integrated H I column density as a function of Galactic longitude and Galactic latitude. If we notice Figure 2.3, we can see that Sightline A unfortunately lies only slightly outside the high-velocity component of the Smith Cloud. However, the high-velocity gas seems to follow the general shape that is expected from the Smith Cloud.

$$\langle v \rangle = \int_{v_{\mathrm{min}}}^{v_{\mathrm{max}}} v \tau_B(v) dv, \tag{2.8}$$

where $\tau_B(v)$ is the normalized brightness temperature. In this **Moment 1 Map**, we see
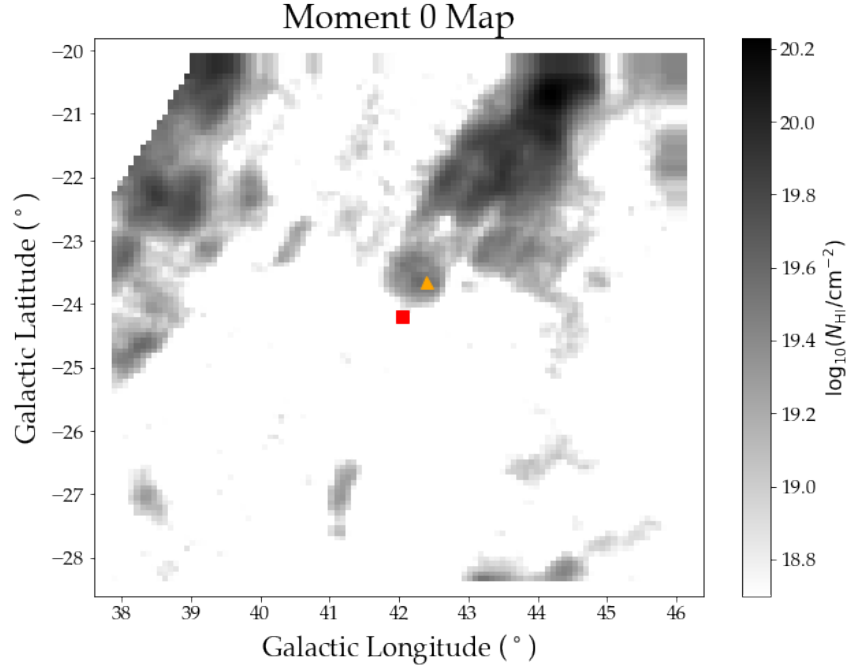
Figure 2.3: The Moment 0 map around Sightline A. The color axis here represents the log of the H I column density. The red square marks Sightline A's location; whereas the orange triangle marks a local maximum in H I column density. The velocity array was masked such as to **only** include $v_{\mathrm{LSR}} \geq +60$ km s^{-1}. Note that there is another Smith Cloud component at $v_{\mathrm{LSR}} \approx +45$ km s^{-1}

similar morphology in the Smith Cloud, but we obtain velocities in a nearby clump of $\langle v_{\mathrm{LSR}} \rangle \approx +110$ km s^{-1}. This is consistent with what we find in the UV data, namely with Si II $\lambda 1190$ and O I $\lambda 1302$. However, there seems to be a steep drop-off in H I column density near the sightline. This likely indicates that the UV absorption along this sightline does indeed correspond to the Smith Cloud high-velocity component.

Since we are confident in the correlation between the kinematics of nearby H I and the UV detections with HST, the next step is to quantify potential limits to the H I detection. Firstly, we fit a Gaussian curve to a nearby high-velocity component at $(\ell, b) = (+42.16°, -24.04°)$, which, assuming a distance of $d = 12.4$ kpc, corresponds to a distance
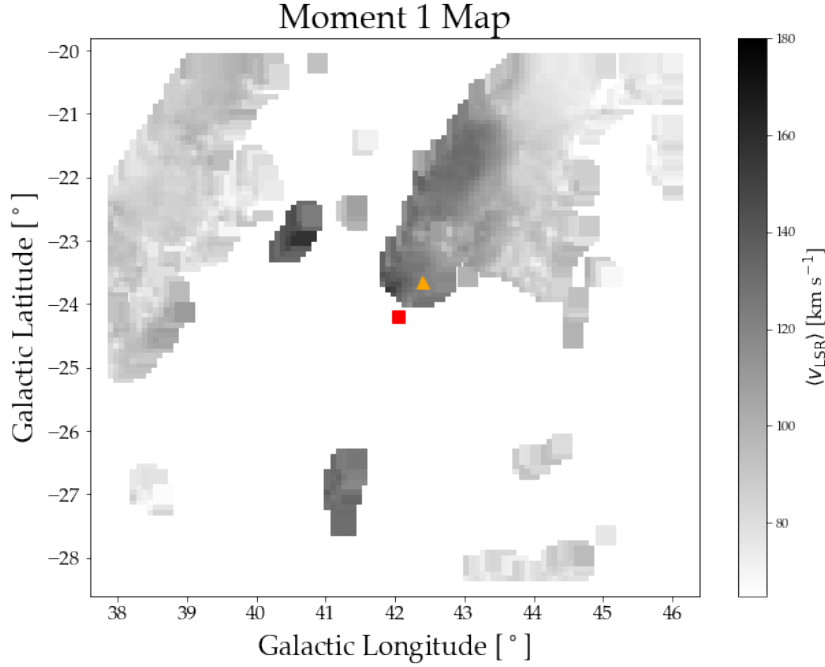
Figure 2.4: Similarly to Figure 2.3, this is a map of integrated average velocity as a function of Galactic longitude and latitude. Once again, Sightline A lies just outside of the H I overdensity.

of $\Delta s \sim 4.9$ pc from the sightline. In Figure 2.6, we overplot a Gaussian to this high-velocity Smith Cloud component. We utilize the center velocity and kinematic full-width at half-maximum (FWHM) in the determination of the H I column density for the GBT sightline corresponding to Sightline A.

Using the following relation, we can derive the FWHM from the Gaussian deviation term from the fit:

$$v_{\mathrm{FWHM}} = 2\sqrt{2\ln 2}\sigma_v \tag{2.9}$$

We then utilize $(v_0, v_{\mathrm{FWHM}}) = (+133.0, 32.1)$ km s^{-1} for the determination of H I column density, as these were the Gaussian parameters fit to a nearby sightline (see Figure 2.6). Before numerically integrating, we must first define a detection limit of
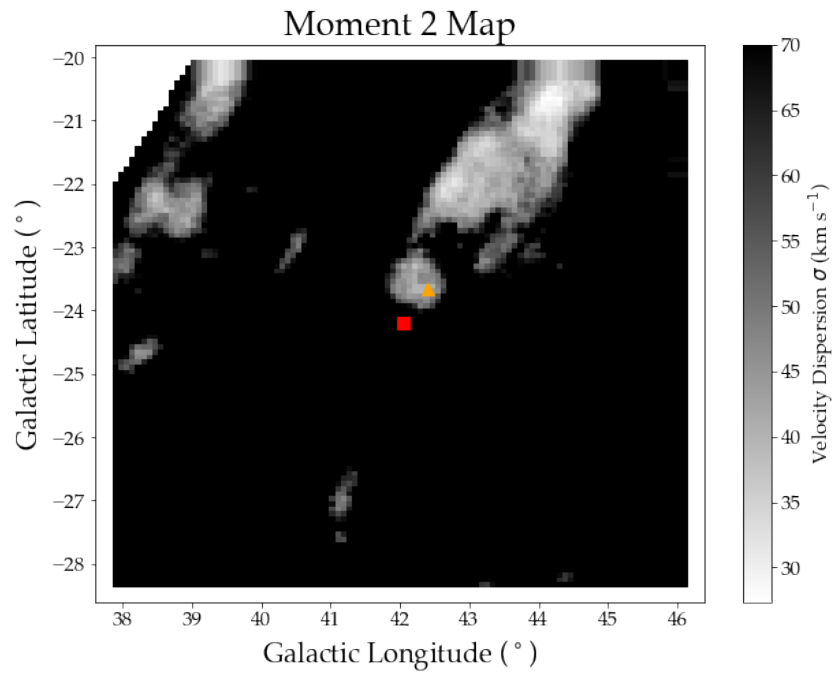
Figure 2.5: Color map of velocity dispersion as a function of Galactic coordinates
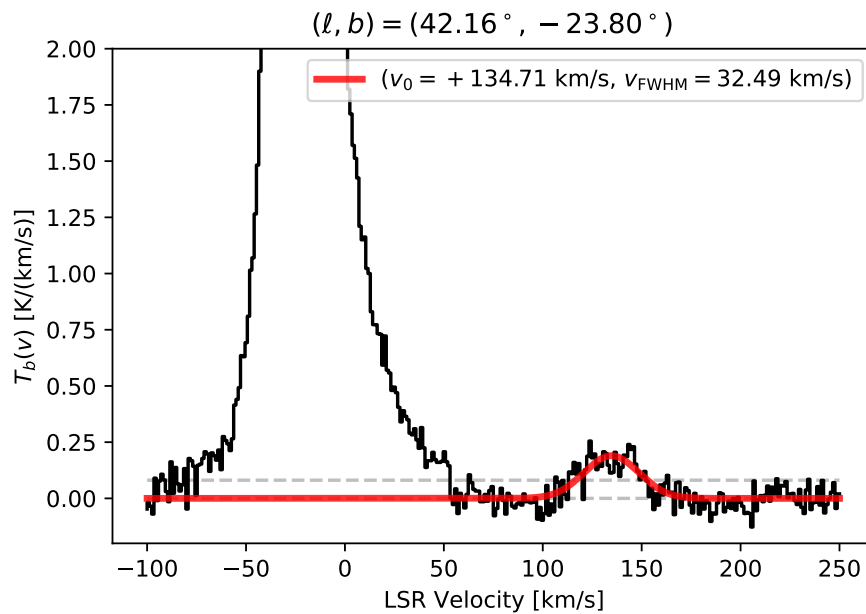
Figure 2.6: Gaussian fit in red to the high-velocity component in the GASS data at a sightline near Sightline A.

H I. We first take the statistical root-mean-square value of the brightness temperature array where there is no obvious signal. We then take a rectangle of the width equivalent to the FWHM derived from the GASS emission line and a height equivalent to the standard deviation of the brightness temperature to derive an H I column density from Equation 2.5. We then perform numerical integration of the brightness temperature from $v_0 - v_{\mathrm{FWHM}}$ to $v_0 + v_{\mathrm{FWHM}}$. For this sightline, we obtain a 3σ noise threshold of $\log N_{\mathrm{H\,I}} = 18.18$ and a signal of $\log N_{\mathrm{H\,I}} = 18.08 \pm 0.55$. We obtained the errorbars from the following relations:

$$\sigma_T = \sqrt{\langle T^2 \rangle}, \tag{2.10}$$

where $\langle T^2 \rangle$ is the average value of T^2 in the noise region.

We then find our error through the following relation:

$$\sigma_{\log N_{\mathrm{H\,I}}} = \frac{\partial \log N_{\mathrm{H\,I}}}{\partial T_b} \sigma_{T_b} = \frac{\sigma_{T_b}}{\langle T_b \rangle \ln(10)} \tag{2.11}$$

This corresponds to a signal-to-noise ratio $[\mathrm{S/N}] = 0.78$. This implies a detection signal in H I that is difficult to distinguish from a 3σ noise limit. These large errorbars in H I detection make metallicity constraints on this sightline difficult. Not only does this effect the raw [S II/H I] measurement, but it also effects the ionization corrections needed to constrain the metallicity. Another source of error for this calculation includes that we use center velocity measurements and FWHM measurements for nearby H I sightlines. This neglects the possibility that the center velocity for this HVC could be significantly different from nearby sightlines. However, the center velocity and FWHM we choose

seem to match well with UV observations.

2.3.2   UVQSJ204402 (Sightline B)

.

Observing Figure 2.1, this sightline lies closer to the main body of the Smith Cloud. This could mean that this sightline is well-shielded by the cloud in front of it, which could yield lower temperatures and more material in lower ionization states. For this sightline, there are two kinematic components of H I. However, the velocity resolution of COS/G130M of FWHM = 15.2 km/s (Fox et al. 2018a) is not high enough to resolve these two components. Therefore, the H I column densities from both components are added together to provide a characteristic $N_{\rm H\,I}$ for this sightline of log $N_{\rm H\,I}$ = 19.53±0.05.

2.3.3   Sightlines C, D, & E

For Sightline C, Fox et al. (2016) found that the the H I (70 km/s) and the S II (58.5± 6.1 km/s) 20 km/s were also kinematically offset. In order to probe the discrepancies between these two velocities, they utilized the LAB Survey's H I observations (Kalberla et al. 2005). They found that the H I emission in the LAB Survey was centered at 62 km/s, which better-matched the S II data for this sightline. However, Fox et al. (2016) did consider this uncertainty and added a 0.10 dex systemic error to their [S II/H I] calculation. For Sightlines D and E, the H I and S II are in good agreement.

Target	Ion	$\log_{10}(N_X/\mathrm{cm}^{-2})$	v_{cen} (km s^{-1})	b (km s^{-1})
A[f]	H I λ21cm (1)[d]	19.21 ± 0.03	$+41.1 \pm 0.6$	12.4 ± 0.1
	H I λ21cm (2)[d]	18.67 ± 0.06	$+46.8 \pm 0.3$	3.4 ± 0.2
	H I λ21cm (3)[d]	< 18.18	$\approx +133.0$	≈ 27.0
	S IIλ1250, 1253, 1259	14.41 ± 0.10	$+123.9 \pm 8.4$	25.0^{a}
	Si III/Si II	> -0.07		
B[f]	H I λ21cm (1)[d]	19.14 ± 0.04	$+58.4 \pm 0.3$	8.3 ± 0.2
	H I λ21cm (2)[d]	19.30 ± 0.04	$+69.1 \pm 1.0$	16.7 ± 0.6
	S IIλ1250, 1253, 1259	15.00 ± 0.16	$+68.3 \pm 9.0$	18.2 ± 11.9
	Si III/Si II	$\sim^{b}$		
C[e]	H I λ21cm	18.84 ± 0.05	$+79$	26.5
	S IIλ1250, 1253, 1259	$+14.38 \pm 0.13$	$+58.5 \pm 6.1$	19.0 ± 10.2
	Si III/Si II	> -0.89		
D[e]	H I λ21cm	18.72 ± 0.06	$+42$	22
	S IIλ1250, 1253, 1259	14.40 ± 0.33	$+41.5 \pm 14.5$	20.0 ± 24.7
	Si III/Si II	$\sim^{b}$		
E[e]	H I λ21cm	19.41 ± 0.02	$+55$	26.5
	S IIλ1250, 1253, 1259	14.17 ± 0.20	$+58.5 \pm 1.1$	8.1 ± 1.8
	Si III/Si II	> -0.99		

Table 2.2: A table of H I and S II column densities with Si III/Si III ratios for all five sightlines in this study.

[a] These values were anchored in the VoigtFit software in order to find the optimal fit that had a reasonable Milky Way and Smith Cloud component.
[b] Both the Si II and Si III lines are saturated, meaning that obtaining a limit on the line ratio for these two ionization species is not possible.
[c] This value is a lower bound on the column density based on the AOD method.
[d] We fit two Gaussian components to the intermediate-velocity component of the Smith Cloud. However, the H I emission that best-matches with the UV is numerically integrated but lies below the 3σ detection limit, which is reported in the column for H I λ21cm (3).
[e] The HST and GBT data for these sightlines were analyzed by Fox et al. (2016) with the vpfit Voigt-fitting package. Additionally, the H I data from these sightlines were numerically integrated (see Equation 2.5).
[f] Additional line profile parameters and additional lines for these two sightlines can be seen in Appendix B.
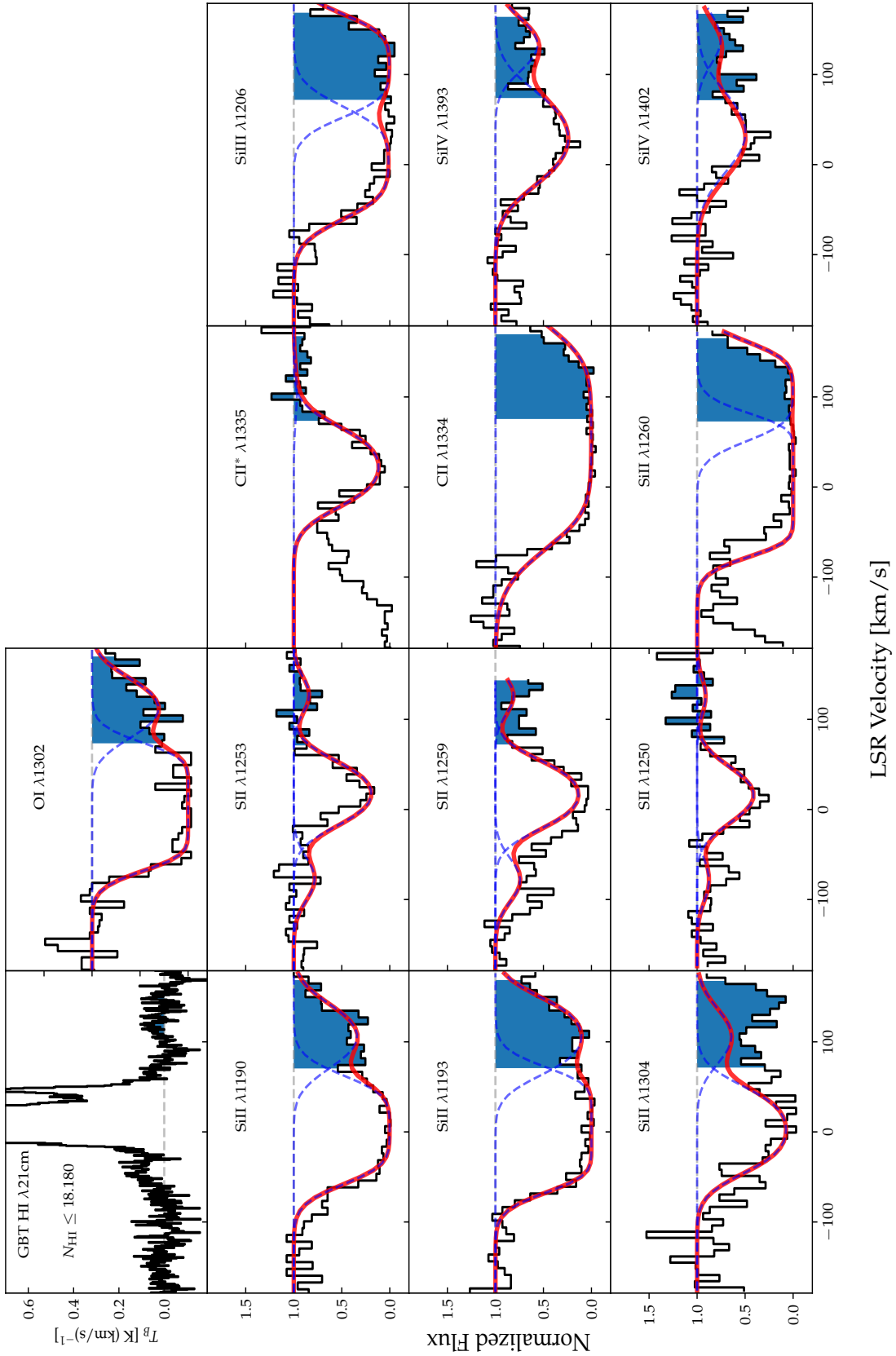
Figure 2.7: Sightline A plotstack. The high-velocity H I on this sightline is below the detection limit, so it is reported as less than the detection limit.
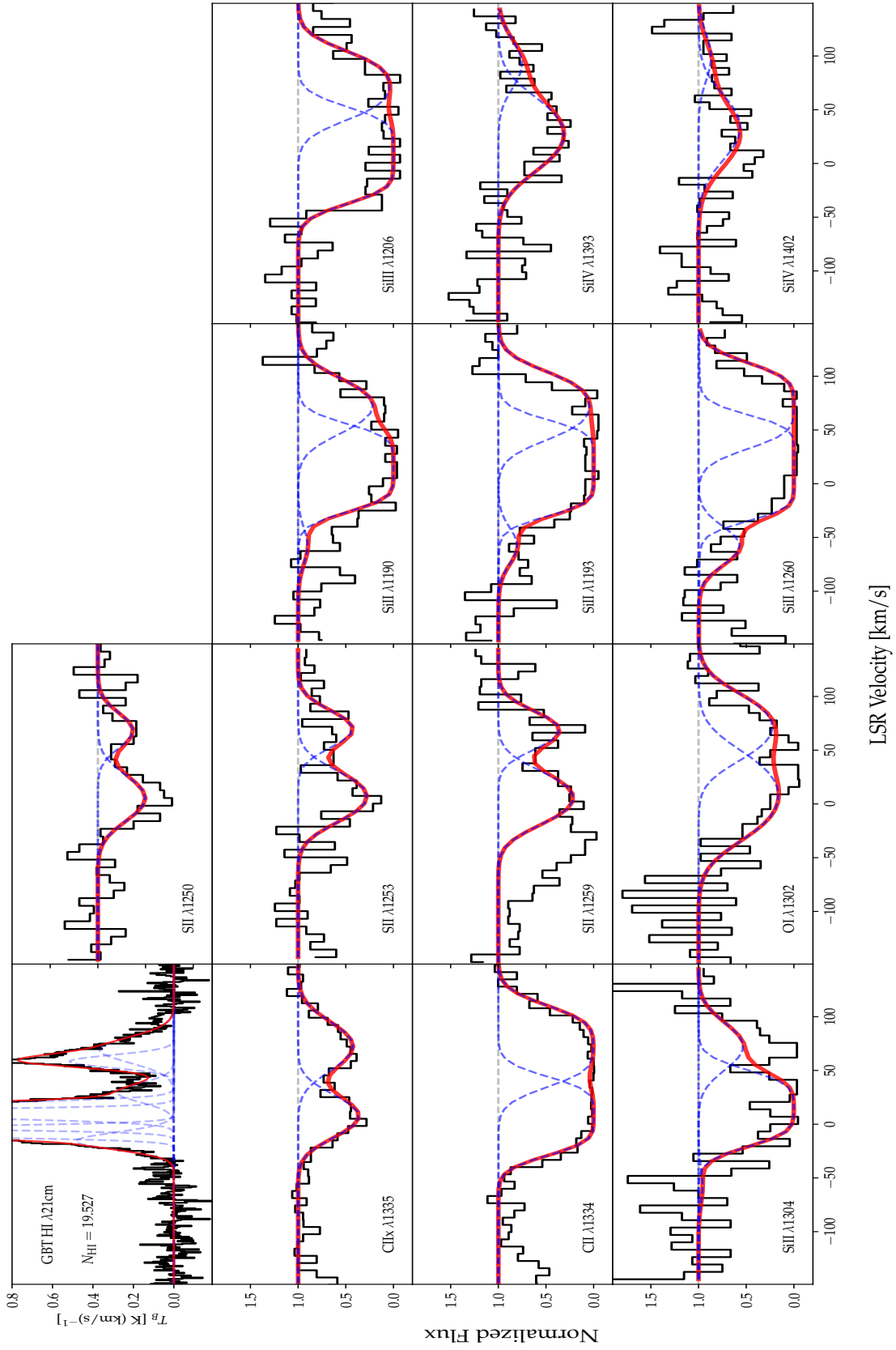
Figure 2.8: Sightline B plotstack. The red line represents the total fit and the blue dotted lines represent individual kinematic components in the spectra.

26
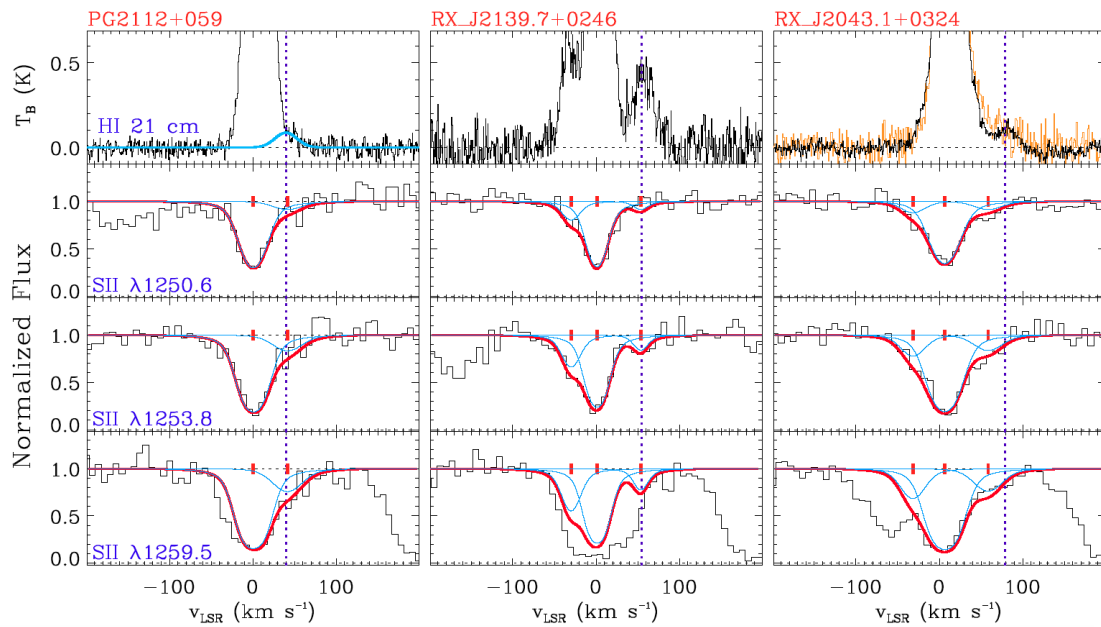
Figure 2.9: Plotstack of the Fox et al. (2016) sightlines. Top to bottom are listed the H I λ21cm emission from GBT and the S IIλ1250, 1253, 1259 from HST/COS/G130M from Fox et al. (2016). From left to right the sightlines are Sightline D, Sightline E, and Sightline C.

Chapter 3

Determination of Chemical

Abundances & Other Physical

Properties

Although direct observation can give us good clues on *some* physical properties of a gas cloud, we must determine other parameters with photoionization simulations. We have seen that the column densities, center velocities, and Doppler parameters can be obtained from observation alone. Although these parameters provide useful information about the cloud, they do not fully provide the information needed for this study. The density within the Smith Cloud is so low that microphysical processes such as photoionization are the main culprit responsible for the spectra that we observe with HST (Ferland et al. 2017). In order to understand the three-dimensional particle density, temperature, pressure, and

ionization of any gas cloud, photoionization simulations must be run to match with the observed properties of the gas cloud.

For this study, we use Ferland et al. (2017)'s photoionization software *Cloudy*. This simulation takes cloud metallicity, neutral hydrogen column density, distance from the observer, location in the sky, and radiation field as input parameters. In order to determine how the Smith Cloud is being disrupted by the Milky Way's halo, we must first understand its chemical composition.

3.1   Metallicity

To determine this chemical composition, or *metallicity*, we utilize both observations and *Cloudy* models. To get an accurate first-order calculation of metallicity, we consider a ratio of two consecutive ionization species of the same element (to avoid metallicity dependence) as well as the column density of neutral hydrogen. Within the observed UV band from COS, the best candidates for the two consecutive ionization species are Si II and Si III, as silicon is the only element with consecutive ionization species in the G130M wavelength range.

In order to determine the metallicity, we ran a grid of *Cloudy* simulations at different values of ionization parameter $U \equiv n_\gamma/n_\mathrm{H}$ at solar metallicity $Z = 0.00$ dex, using the extragalactic background radiation field from Khaire & Srianand (2019) and the Milky Way radiation field from Bland-Hawthorn & Maloney (2001). Next, we compared the results of the $N_\mathrm{Si\,III}/N_\mathrm{Si\,II}$ ratio to the n_H grid values to determine the range of possible n_H values. We then compared this range of n_H values to the ionization correction for

sulfur since it does not deplete onto dust grains and has a similar ionization potential to hydrogen (Draine 2011). We use sulfur, as it does not deplete onto dust grains , and has a similar ionization potential to hydrogen Draine (2011). The ionization correction for sulfur is

$$IC(S) \equiv [S/H] - [S\ \textrm{II}/H\ \textrm{I}], \tag{3.1}$$

where [S/H] is the true sulfur abundance and [S II/H I] is the relative abundance of S II to H I compared with the Sun, such that

$$[S\ \textrm{II}/H\ \textrm{I}] \equiv \log N_{S\ \textrm{II}} - \log N_{H\ \textrm{I}} - \log (S/H)_{\odot}, \tag{3.2}$$

with $(S/H)_{\odot}$ being the ratio of sulfur to hydrogen in the Sun (Fox et al. 2016; Fox et al. 2018b; Asplund et al. 2009). Note that the Si III/Si II ratio is a lower limit for three of our sightlines, since the Si III line is saturated due to its high oscillator strength.

3.1.1 Ionization Correction/log(U) Dependence

The ionization potential of hydrogen is $E_{H\ \textrm{I}\longrightarrow H\ \textrm{II}} = 13.5984$ eV and the first and second ionization potentials of sulfur are $E_{S\ \textrm{I}\longrightarrow S\ \textrm{II}} = 10.3600$ eV and $E_{S\ \textrm{II}\longrightarrow S\ \textrm{III}} = 23.3379$ eV, respectively (Draine 2011). S II will likely exist in a similar gas phase to H I, since both will exist in low-ionization regions. However, if we compare the ratio of S II/H I, we will not have the same ratio as the true (S/H) of the cloud. This is because S I **also** traces H I, meaning that we must correct for the relative ionization of hydrogen and sulfur.

This ionization correction (IC) is simply an additive term in log space (whereas it is

called an ionization correction factor when used in linear space and is multiplicative to the S II/H I ratio).

$$[\text{S/H}] = [\text{S II/H I}] + \text{IC(S)} \tag{3.3}$$

The ionization correction term is always negative. (S II/H I) is greater than the true (S/H) ratio Fox et al. (2018b). Since the second ionization potential of sulfur is much greater than that of hydrogen's ionization potential, more S II exists compared to H I. To derive this ionization correction, a parameter describing the ionization of the gas must be used.

This ionization parameter has a simple closed form (ionization parameter $U = n_\gamma/n_{\text{H}}$, where $n_\gamma = \#$ density of ionizing photons of hydrogen and $n_{\text{H}} = \#$ density of total hydrogen). Ideally, this ionization parameter would be derived from the ratio of Si III/Si II, as was done in Fox et al. (2016) for sightlines C and E; however, on sightlines A and D, both Si II and Si III are saturated, implying that a limit for this ratio is not feasible. Therefore, finding limits for the physical parameters is, unfortunately, not achievable on these sightlines either.

To find the limits of each physical parameter, we plot the Si III/Si II ratio on the y axis and the physical parameter of interest on the x axis. We then find where the best-fit polynomial crosses over the lower limit Si III/Si II value and take that value as our limit. We complete this analysis for $\log U$ (dimensionless units), $\log \chi_{\text{H I}}$ (dimensionless units), $\log n_e$ (electrons cm^{-3}), $\log n_{\text{H}}$ (atoms cm^{-3}), $\log(T)$ (K), $\log[P/k]$ (K cm^{-3}), $\log L$ (kpc). In this chapter, we provide an example plot of one such derivation (see Figure 3.1). The rest of the The remaining derivation plots can be found in Appendix A.
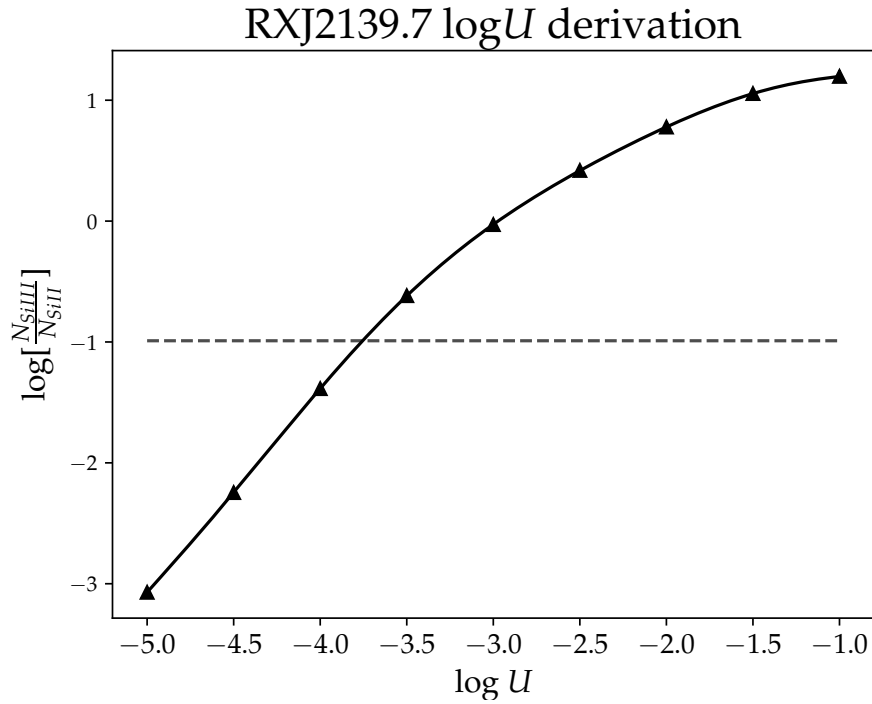
Figure 3.1: The derivation of ionization parameter U on sightline E. On the x-axis is $\log U$ and on the y axis is $\log \frac{N_{\mathrm{Si\,III}}}{N_{\mathrm{Si\,II}}}$. Here we use a limit of $\frac{N_{\mathrm{Si\,III}}}{N_{\mathrm{Si\,II}}} > -0.99$, derived in Fox et al. (2016). The dashed black line represents the **_lower limit_** on the ionic ratio. Therefore, this is a lower limit on the ionization parameter of $\log U > -3.43$
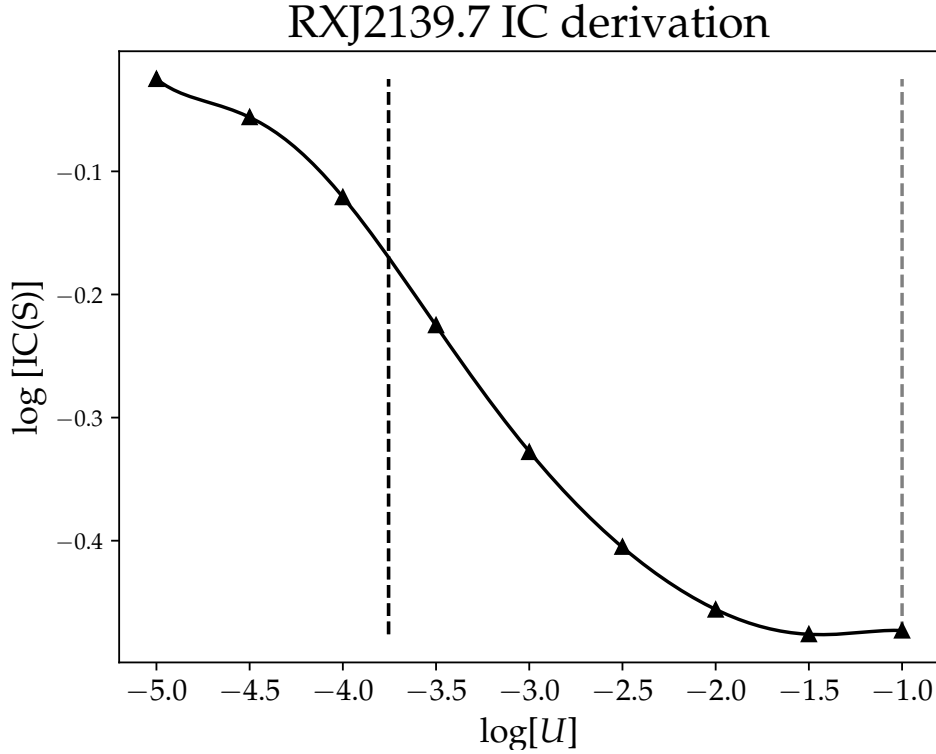
Figure 3.2: On the x axis is the ionization parameter U and the y axis describes the ionization correction factor of S II to obtain the metallicity. The dashed black vertical line is the minimum value of $\log U$ derived from the observed $\frac{N_{\text{Si III}}}{N_{\text{Si II}}}$ ratio. The second dashed line is approximately the minimum value of the IC from *Cloudy* simulations for Sightline E.

The relation between IC and U depends only on U and the neutral hydrogen column density $N_{\text{H I}}$ (Fox et al. 2016; Fox et al. 2018b). Luckily, this relation also asymptotes to different IC values at extreme values of U (see Figure 3.2). For instance, at high U values $\log U \sim -1.0$, which correspond to a high density, the IC will asymptote to its lowest value. However, for $\log U \sim -5.0$, the curve asymptotes to its highest value (usually IC = 0.00). These asymptotes are also largely independent of metallicity, making this method incredibly useful for placing upper and lower bounds to the metallicity of the Smith Cloud.

We apply the following bounds to the metallicity using this curve:

1. **Lower bound**

   (a) Add the minimum IC to the best-fit [S II/H I]

   (b) Propagate error in the UV S II Voigt fit and the H I Gaussian fit.

   (c) subtract the propagated error

   (d) $Z_{\min} =$[S II/H I] + $IC_{\min}$ - σ

2. **Upper bound**

   (a) Add the minimum IC to the best-fit [S II/H I]

   (b) Add the propagated error from part 1 to [S II/H I]

   (c) $Z_{\max} =$[S II/H I] + $IC_{\min}$ + σ

For the expectation value of the metallicity, we simply report the average of the lower and upper bounds of the metallicities derived from the previous two methods. For the errorbars, we take the maximum value of the IC and add in the observational error and a 0.10 dex beam smearing error in quadrature. Since the errorbars on Sightline A and Sightline D are so large, we must consider a weighted average and weighted deviation of [S/H]. Using analysis methods discussed in Taylor (1997) and Cohen et al. (2003), we find [S/H] $= -0.60 \pm 0.33$, correlating to $Z = 0.25 \pm 0.19 Z_{\odot}$. We report the weighted average $\bar{Z}^*$ and weighted standard deviation σ_Z^* as

$$\bar{Z}^* = \frac{\sum_i w_i Z_i}{\sum_i w_i}; \ w_i \equiv \frac{1}{\sigma_i^2}, \tag{3.4}$$

and

$$\sigma_Z^* = \sqrt{\frac{\sum_i w_i(Z_i - \bar{Z}^*)^2}{\frac{N-1}{N}\sum_i w_i}} \tag{3.5}$$

where Z_i are the mean metallicity observations, w_i are the statistical weights, and $N = 5$ is the number of observations. Note that to derive the weighted average and weighted deviation of the metallicity, we convert the logarithmic metallicities and logarithmic errors into linear space via the relation given in Taylor (1997):

$$\sigma_{Z_{\mathrm{lin}}} = \frac{\partial Z_{\mathrm{lin}}}{\partial \log_{10} Z}\sigma_{\log Z} = (\ln 10)Z_{\mathrm{lin}}\sigma_{\log Z} \tag{3.6}$$

3.1.2 Linear Regression Fitting

We perform a reduced-chi-squared ($\tilde{\chi}^2$) analysis on the best-fitted line to provide an error envelope for the best-fit lines. To calculate $\tilde{\chi}^2$, we use the following equation from Taylor (1997):

$$\tilde{\chi}^2 = \frac{1}{\mathrm{d.o.f}}\sum_{i=1}^{N}\left(\frac{p_i - Z_i}{\sigma_i}\right)^2, \tag{3.7}$$

where N is the number of data points ($N = 5$); the degrees of freedom (d.o.f) is equal to $N - 2$, since a line has two fitted values ($mx + b$); p_i is the ith value of the fitted polynomial; Z_i is the ith median value of [S/H]; and σ_i is the ith errorbar on [S/H]. For Sightline A, since the [S/H] measurement is a lower limit, we choose a flat distribution in our Monte Carlo runs, choosing an upper limit of [S/H] $< +0.30$ while using the *Cloudy*-derived lower limit on [S/H]. The error envelopes provided show the lines that exist within the $\tilde{\chi}^2_{\mathrm{min}} + 1$ and $\tilde{\chi}^2_{\mathrm{min}} + 2$ regions, where $\tilde{\chi}^2_{\mathrm{min}} = 0.22$. Although this value
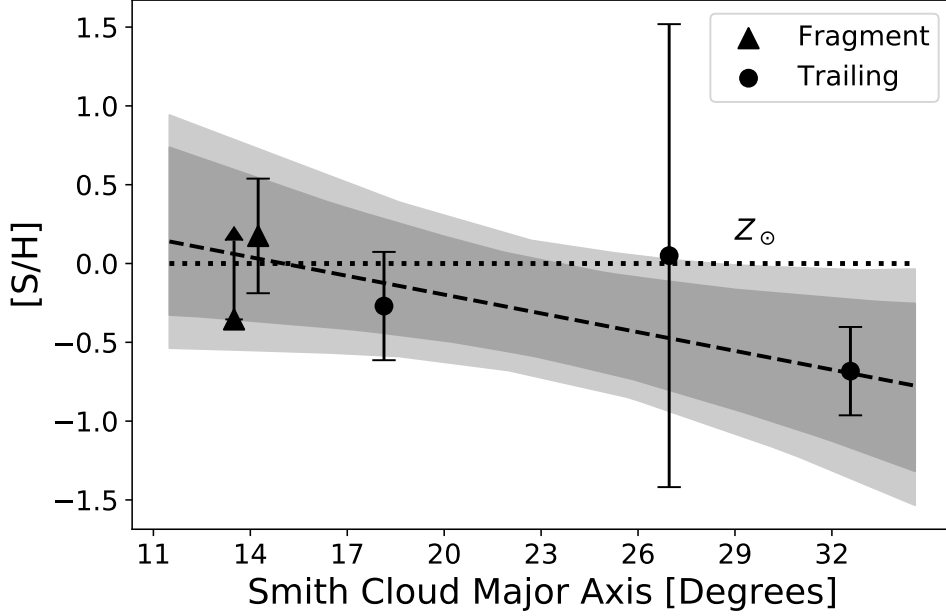
Figure 3.3: On the x-axis is the Smith Cloud major axis component of the distance from the head of the Smith Cloud with 1σ errorbars. The y-axis contains [S/H] estimates for each sightline. The sightlines (from left-to-right) are A, B, C, D, and E. The dotted line represents solar metallicity while the dashed line represents the best-fit metallicity gradient of the Smith Cloud. The darker colored-in area represents the area in which there are fitted lines with $\tilde{\chi}^2 < \tilde{\chi}^2_{\min} + 1$. The lighter colored-in area represents the area in which there are fitted lines with $\tilde{\chi}^2 < \tilde{\chi}^2_{\min} + 2$.

is less than 1, this smaller value is to be expected for a small sample size.

3.1.3 Results

[S/H] abundnace seems to decrease as we look further "downstream" in the Smith Cloud

(see Figure 3.3; Table 3.2). In fitting a line to the data, we find a linear correlation of log

[S/H] $=(-0.040 \pm 0.041)\mu + (0.60 \pm 0.80)$, where μ represents the major axis coordinate.

Fox et al. (2016) first noticed this potential trend in the metallicity downstream in the

Smith Cloud. These two new sightlines re-affirm this. The two sightlines within a

condensed clump (sightlines A and B) also show a higher metallicity than the downstream

gas.

However, we must also consider a few observational differences in these sightlines. For Sightline A, recall that the H $\text{\textsc{i}}$ column density was below the 3σ detection limit. A lower H $\text{\textsc{i}}$ column density could imply an even higher metallicity than we estimated. Additionally, the sulfur IC is very sensitive to $\log U$ from $\log U \in [-2, 0]$, which makes metallicity estimation difficult at low $N_{\text{H \textsc{i}}}$. However, for Sightline B, despite having saturated Si $\text{\textsc{ii}}$ and Si $\text{\textsc{iii}}$ lines, the ionization correction is well-bounded at high $N_{\text{H \textsc{i}}}$, which makes metallicity estimates more feasible. However, for sightline D, we neither have well-resolved Si $\text{\textsc{ii}}$ and Si $\text{\textsc{iii}}$ lines nor high $N_{\text{H \textsc{i}}}$.

For the weighted average and weighted deviation of the metallicity, we find that [S/H] = -0.598 $\pm$0.330. Some of the re-calculated metallicities and errorbars seem to differ from Fox et al. (2016). Although Fox et al. (2016) also utilized the IC vs. $\log U$ curves for their calculations, their method of calculation differs from ours in the following ways:

1. Fox et al. (2016) utilizes the extragalactic background (EGB) radiation field from Bland-Hawthorn & Maloney (1999); whereas, in this study, we utilize the EGB from Khaire & Srianand (2019). However, this contribution to the ionization parameters would be small, since the radiation incident on the Smith Cloud is dominated by the Milky Way

2. We utilize the 2017 release of *Cloudy*, whereas Fox et al. (2016) utilizes the 2013 release of *Cloudy*. This could explain the discrepancy in $\log U$ calculation for the same sightlines.

3. Fox et al. (2016) utilizes the lower limit of $N_{\text{Si \textsc{iii}}}/N_{\text{Si \textsc{ii}}}$ to derive $\log U$ and implement

a 0.1 dex error on $\log U$. We instead utilize the method in Fox et al. (2018b), where U is taken to be a limit.

4. Since we are interested in the physical parameters of the cloud, we do not implement a $\log U$ value for sightlines A and D (the sightlines without a silicon ionization ratio) as did Fox et al. (2016).

3.2   Other Physical Properties

As the Si III lines are saturated for all five sightlines, the ionization conditions of the Smith Cloud will be in the form of a limit. More specifically, since the Si III/Si II ratio is in the form of a lower limit, conditions that increase with increased ionization (such as temperature, $\log U$, etc) will also have lower limits. However, ionization-mitigating conditions like $\chi_{\mathrm{H\,I}}$ and n_{H} will have an upper limit.

Similarly to the method for determining $\log U$, we plot ionization parameters against the $N_{\mathrm{Si\,III}}/N_{\mathrm{Si\,II}}$ ratio. We fit an order 5 polynomial to the data from the simulations and find the point where ionic ratio as a function of the parameter crosses over the observed limit (see Figure 3.4). For each sightline with a limit on the $N_{\mathrm{Si\,III}}/N_{\mathrm{Si\,II}}$ ratio, we find the upper or lower limits on each ionization condition in a similar manner. Similarly to the metallicity, we plot each ionization condition as a function of major axis coordinate. Below we provide an example for the density of neutral hydrogen (see Figure 3.5).

In this figure, we might notice an increase in the density along the length of the Smith Cloud. However, recall that Sightline A has a high uncertainty in the $N_{\mathrm{H\,I}}$ measurement. This could be the culprit for the small upper limit of n_{H}. We find for this sightline an
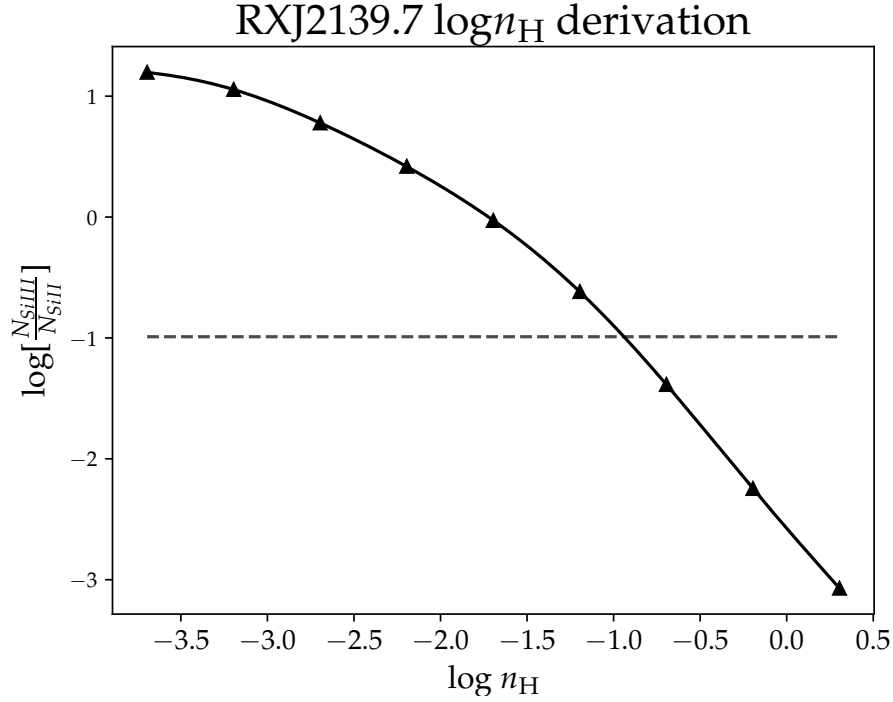
Figure 3.4: The x axis is total hydrogen particle density and the y axis is the $N_{\text{Si III}}/N_{\text{Si II}}$ ionic ratio. The dashed line is the measured limit on this ratio for sightline E.

Target	$\frac{N_{\text{Si III}}}{N_{\text{SiII}}}$	$N_{\text{H I}}$	n_γ
A	$\sim^a$	19.53 ± 0.05	-4.499
B	> -0.068	18.08 ± 0.52^b	-4.715
C	> -0.99	19.41 ± 0.02	-4.695
D	$\sim^a$	18.72 ± 0.06	-4.695
E	> -0.89	18.84 ± 0.05	-4.715

Table 3.1: Inputs into the *Cloudy* simulations.
^{a} The Si III/Si II ratios could not be determined on these sightlines due to line saturation.
^{b} This H I column density was determined with Monte Carlo integration due to a small [S/N] ratio.

average $\log n_{\mathrm{H}} > -1.48$, which matches previous observations of this region of the Smith

Cloud with the Wisconsin Hα Mapper (WHAM; Hill et al. 2013).

3.3   Results

Targ.	$N_{\mathrm{H\,I}}$	[S II/H I]	$\frac{N_{\mathrm{Si\,II}}}{N_{\mathrm{Si\,III}}}$	U	IC(S)	[S/H]
A	< 18.18	$> +1.109$	> -0.07	$> -2.71^d$	-1.40, 0.00^d	$+0.44 \pm 0.82^c$
B	19.53 ± 0.05	$+0.35 \pm 0.19$	$\sim^a$	$\sim^b$	-0.34, 0.00	$+0.18 \pm 0.36$
C	18.84 ± 0.05	$+0.42 \pm 0.13$	> -0.89	> -3.43	-0.82, -0.52	-0.27 ± 0.34
D	18.72 ± 0.06	$+0.56 \pm 0.33$	$\sim^a$	$\sim^b$	-0.94, 0.00	$+0.05 \pm 1.46$
E	19.41 ± 0.02	-0.36 ± 0.20	> -0.99	> -3.54	-0.46, -0.18	-0.68 ± 0.26

Table 3.2: A table of some observational measurements and *Cloudy*-derived quantities important for determining the metallicity. All values are reported in log space. The H I column density is in units of cm^{-2}, and the ionization corrections are reported as lower limits and upper limits.
^{a} We were not able to determine these ratios due to line saturation and kinematic blending with the Milky Way.
^{b} Since we could not find a silicon ionization ratio, we could not constrain the ionization parameter U nor could we constrain any other ionization condition besides ionization correction.
^{c} Here, the errorbar represents the uncertainty that comes from the ionization correction fit to a 3σ H I detection of $\log N_{\mathrm{H\,I}} = 18.18$. More precisely, the lower limit of the abundance is [S/H] > -0.38
^{d} These values were derived for a simulation run of $\log N_{\mathrm{H\,I}} = 18.18$.

Targ.	n_{H}	n_e	$\chi_{\mathrm{H\,I}}$	$\chi_{\mathrm{H\,II}}$	T_4	P/k	L
A^a	< 0.009	< 0.010	0.000,0.012	0.99,1.00	> 0.589	< 126	> 3.98
C	< 0.052	< 0.044	0.000,0.185	0.82,1.00	> 0.688	< 723	> 0.23
E	< 0.114	< 0.053	0.000,0.455	0.55,1.00	> 0.646	< 933	> 0.12

Table 3.3: *Cloudy*-derived ionization parameters. Sightlines B and D do not appear in this table, as they do not have constraints on the silicon ionization ratio. All values are reported in linear space. The following units are reported:(1) densities n_{H} and n_e are cm^{-3}, (2) T_4 is reported in 10^4 K, (3) P/k is reported in K/cm^3, and L is reported in kpc. Neutral and ionization fractions have hard lower and upper bounds respectively. These upper and lower bounds are reported with a comma between the *Cloudy*-derived limit.
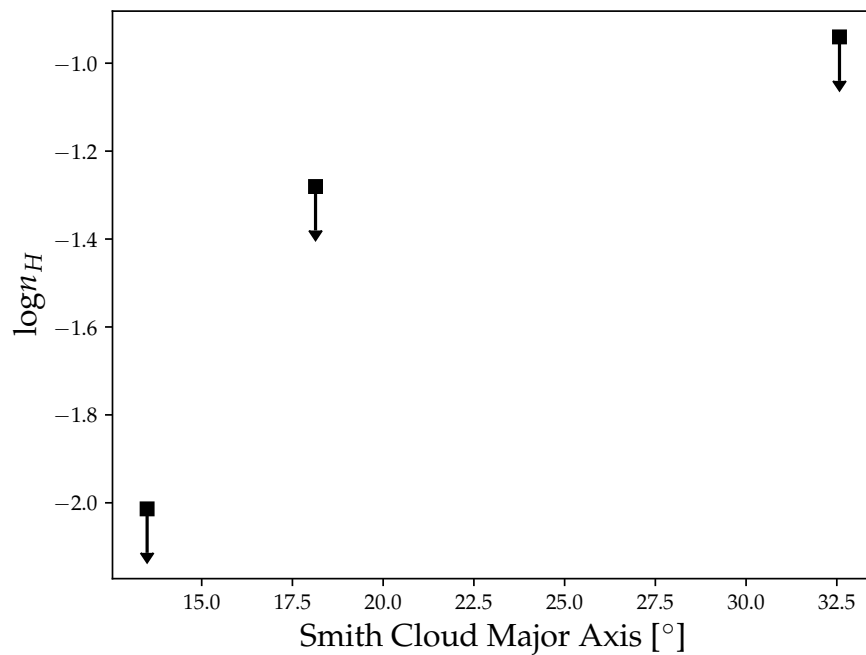^{a} These values were derived for a simulation run of $\log N_{\mathrm{H\,I}} = 18.18$.

Figure 3.5: The x axis here is the major axis of the Smith Cloud and the y axis is the upper limit for $\log n_{\mathrm{H}}$. From left to right the sightlines are sightlines B, C, and E.

Chapter 4

Discussion & Conclusion

In this thesis, we use photoionization modeling and absorption-line spectroscopy to probe the ionization conditions of the Smith Cloud. We find that the metallicity decreases further downstream of the main body of the Smith Cloud. However, the correlation in ionization conditions with the major axis coordinate is weaker. In this chapter, we discuss the implications of these results on the origin of the Smith Cloud and its survivability on its return journey to the Milky Way's Galactic plane. We also discuss potential physical processes that may cause these results.

4.1   Kinematics of the Smith Cloud

We find, for most of our sightlines, a clear intermediate-velocity component around +70 km/s. We also find a high-velocity component for the Smith Cloud at Sightline A in addition to an intermediate-velocity component. However, weak H I emission for this sightline makes determining the kinematic offset between the H I and UV lines difficult.

In observing nearby sightlines in the Smith Cloud, we find an obvious high-velocity component at $v_{\mathrm{LSR}} \approx +133$ km/s. This matches with the kinematic analysis in Lockman et al. (2008), which finds two velocity components in this region of the Smith Cloud.

4.2 Implications on the Halo Mixing & Survivability of the Smith Cloud

In this study, we find a mean metallicity of [S/H] = -0.598 ±0.330, translating to about 25.3% of the Sun's metallicity. This weighted metallicity average is lower than the previous measurement of the sulfur abundance by Fox et al. (2016), most likely due to this study using a weighted average and deviation. We also find a gradient of metallicity along the major axis of the Smith Cloud that decreases with distance from the main body. This decreasing metallicity gradient could imply that the gas in the tail of the Smith Cloud is more easily mixing with the Milky Way's halo and that the main body could have a higher metallicity than the tail.

Henley et al. (2017) explored the observational effects of the Smith Cloud mixing with the Galactic halo. They also considered that the halo could have a high metallicity (near solar). They argued that (1) either the metallicity of the halo is high and the metallicity of the Smith Cloud is low or (2) the metallicity of the halo is low and the metallicity of the Smith Cloud is high. They argued that, due to measurements of high metallicity in the Galactic halo, the metallicity of the Smith Cloud might instead **increase** more downstream from the head. However, in this thesis, we find the opposite. This result could

prove useful for theorists, as it provides a more robust trend of decreasing metallicity downstream in the Smith Cloud.

In this study, we also probed into many of the ionization conditions of the Smith Cloud and find that parts of the tail are at least 46.5% ionized. However, the Smith Cloud seems to be *more* ionized as we approach the main body. However, we must take that result with caution, as the H I on Sightline A is below the 3σ detection limit. Since we were unable to determine a limit on any ionization conditions for Sightlines B and D, a trend is difficult to surmise from the limited available data . This ionization is also a curious result as we might expect the gas to become more ionized the further away the sightline is from the main body since the metallicity decreases with distance from the main body.

For the high-velocity component of the Smith Cloud on Sightline A, we find that a total hydrogen number density of $n_\mathrm{H} < 0.009$ cm^{-3}. We may expect a density near this value for low-density regions of the Smith Cloud (Hill et al. 2009). This could indeed be the region we are probing on Sightline A, as the intermediate-velocity component of the Smith Cloud is too kinematically blended with the Milky Way in UV to make a reasonable determination of the properties of the metals. Interestingly, the density does seem to increase with distance from the main body. However, as previously mentioned with ionization fraction, this trend could be due to the selection of sightlines we have available, most notably for Sightline A.

N-body simulations such as Armillotta et al. (2017) and Tepper-García & Bland-Hawthorn (2018) find that clouds with a size and mass close to that of the Smith Cloud are able to survive their journeys to the Galactic plane. Armillotta et al. (2017), for

instance, considered HVCs with metallicities of 30% of the Sun's and hydrogen number densities of $n_{\rm H} \approx 10^{-2}$ cm^{-3}. As our derived upper limits of densities from photoionization simulations match the densities from Armillotta et al. (2017), the Smith Cloud seems likely to survive its journey to the Milky Way galaxy. However, further hydrodynamic simulations for the Smith Cloud are needed.

4.3   Sources of Error

Some of the metallicity calculations given in this thesis have very large errorbars, impacting what we can say about the physical conditions of the Smith Cloud. Along Sightlines B and D, there are not adequate Si II and Si III measurements. This, unfortunately, means that we cannot reliably constrain the ionization fraction, density, temperature, and other ionization-dependent parameters. Additionally, the H I column density on Sightline A was slightly below the 3σ detection limit, which could limit what can be said on constraints on ionization corrections and other ionization conditions. Additionally, at low H I column densities, the sulfur IC is highly sensitive to small changes in ionization parameter U, further reducing the confidence in our measurements.

4.4   Conclusion

This thesis aimed to answer the following scientific questions:

1. What are the limits of the metallicity, density, pressure, temperature, and ionization within the Smith Cloud?

2. Do these conditions change as a function of the major axis of the Smith Cloud?

We find a decrease in metallicity from the adjacent cloud fragments to the trailing wake of the Smith Cloud. This seems to match Fox et al. (2016)'s initial analysis. We have also quantified this trend into a linear fit. This implies that the tail could be mixing with a low-metallicity Galactic halo. This trend might additionally imply that the main body of the Smith Cloud may have an even higher metallicity than the $\log[S/H] = +0.18 \pm 0.36$ on sightline A. Despite the metallicity's decreasing trend downstream in the Smith Cloud, the ionization conditions were more difficult to constrain.

For the three sightlines with limits on the ionization conditions, a trend with the major axis of the Smith Cloud is not as obvious as with metallicity. These limits of ionization parameters, such as density, ionization fraction, and ionization parameter, were inhibited by kinematic blending and saturation in the UV absorption lines. However, we still provide useful estimates for these physical properties in low, medium, and high H I column density regions of the Smith Cloud.

These new constraints will allow theorists to better understand the future trajectory. Although theoretical studies on the Smith Cloud's future trajectory already exist (Henley et al. 2017; Tepper-García & Bland-Hawthorn 2018), the presence of this study will promote a deeper understanding of the physical processes that may have caused the Smith Cloud to exist and the physical processes this HVC is undergoing and will undergo as it traverses the Galactic Halo.

Appendix A

Images

In this appendix, we provide plots relating to the derivation of ionization parameters from the Si III/Si II ratio. We additionally provide the plots of the ionization parameter limits as a function of Smith Cloud major axis.
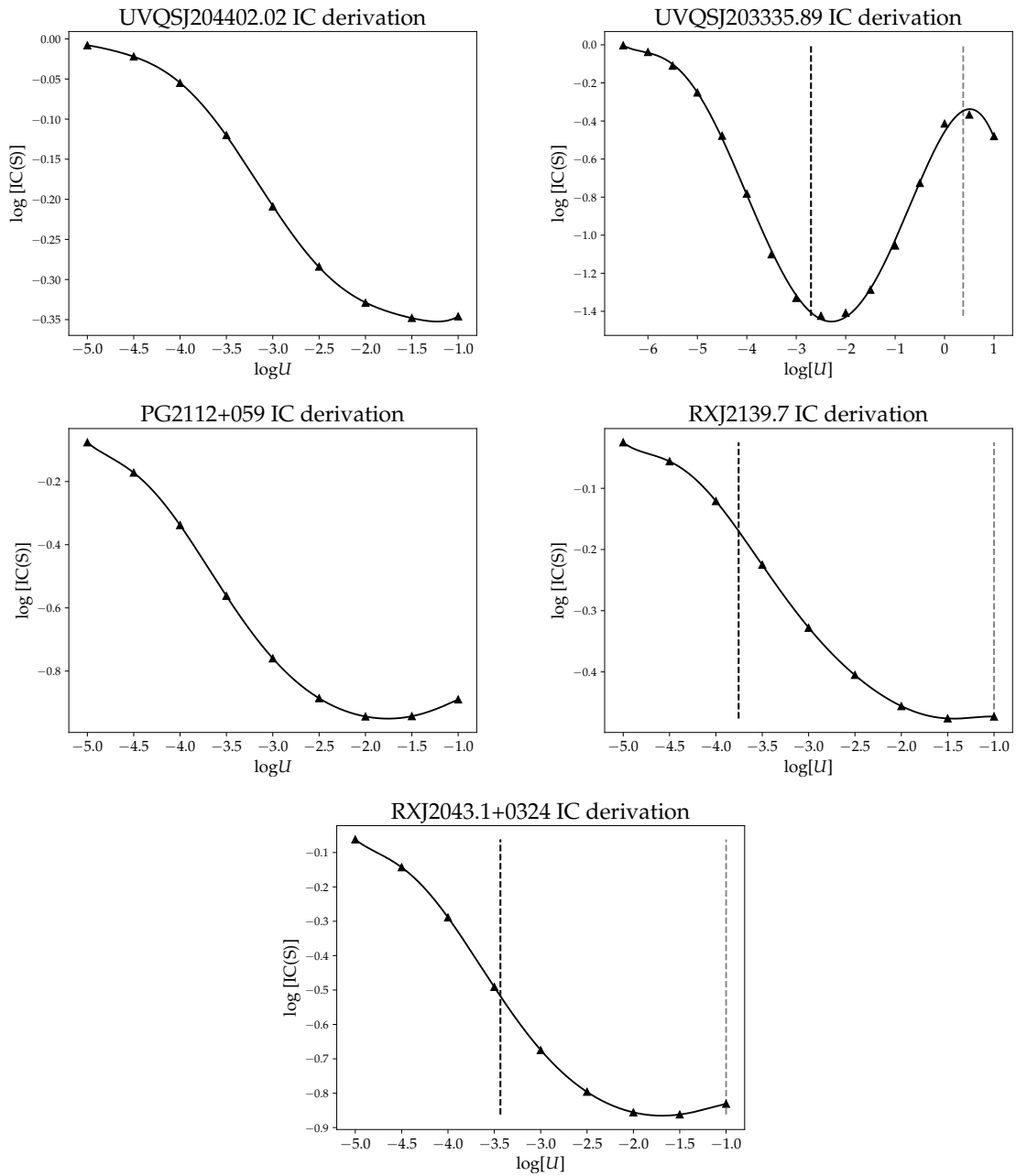
Figure A.1: This plot relates the Ionization Correction (IC) of sulfur with respect to [S II/H I] to the ionization parameter. Notice how the curve asymptotes to 0.00 for small U values and to a minimum for large U values. This trend doesn't hold, however, for sightlines A and D, due to their low H I column density.
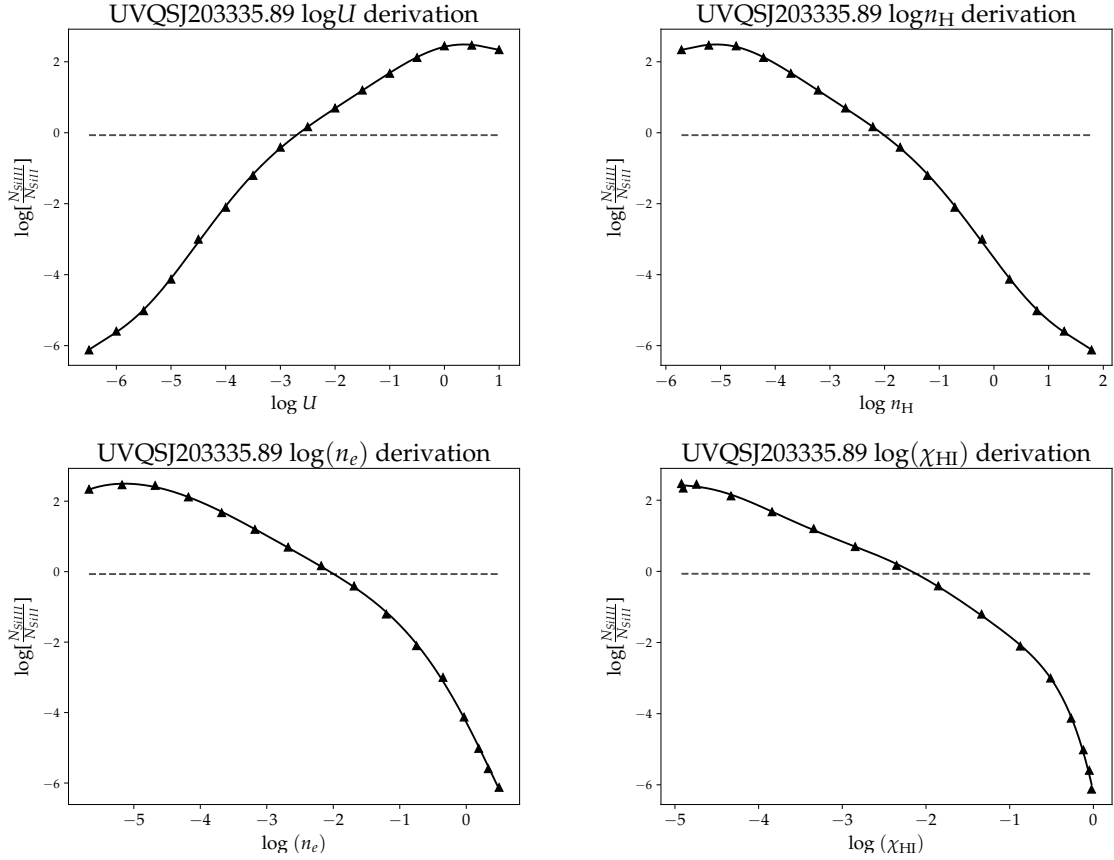
Figure A.2: Above, we plot the derivation of the following physical properties for Sightline A: (top left) ionization parameter, (top right) total hydrogen number density in cm^{-3}, (bottom left) electron density in cm^{-3}, and (bottom right) neutral hydrogen fraction. They are matched to $\log(N_{Si\ III}/N_{Si\ II}) > -0.07$. All values are plotted in log space.

Figure A.3: Above, we plot the derivation of the following physical properties for Sight-line A: (top left) pressure divided by the Boltzmann constant in K cm^{-3}, (top right) temperature in K, and (bottom) line-of-sight length in kpc. They are matched to $\log(N_{\text{Si III}}/N_{\text{Si II}}) > -0.07$. All values are plotted in log space.

Figure A.4: Above, we plot the derivation of the following physical properties for sightline C: (top left) ionization parameter, (top right) total hydrogen number density in cm^{-3}, (bottom left) electron density in cm^{-3}, and (bottom right) neutral hydrogen fraction. They are matched to $\log(N_{\text{Si III}}/N_{\text{Si II}}) > -0.89$. All values are plotted in log space.
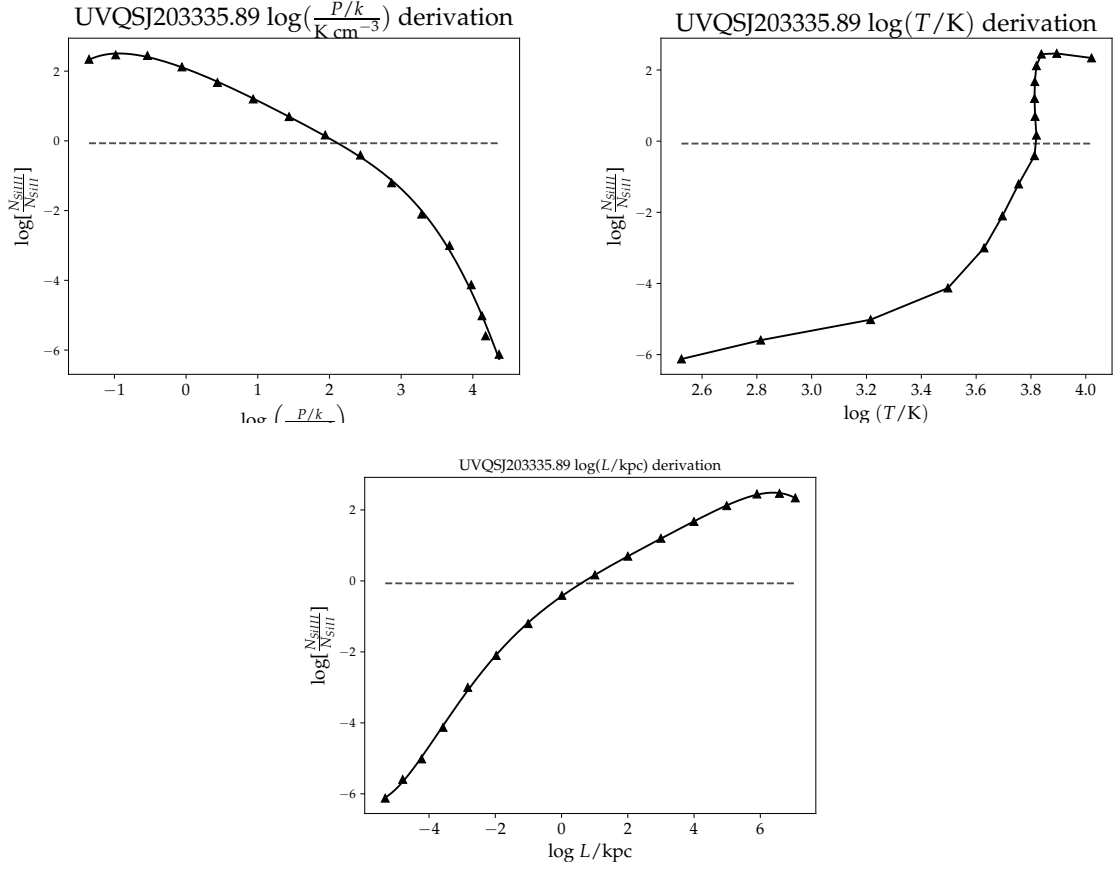
Figure A.5: Above, we plot the derivation of the following physical properties for sight-line E: (top left) pressure divided by the Boltzmann constant in K cm^{-3}, (top right) temperature in K, and (bottom) line-of-sight length in kpc. They are matched to $\log(N_{\text{Si III}}/N_{\text{Si II}}) > -0.89$. All values are plotted in log space.
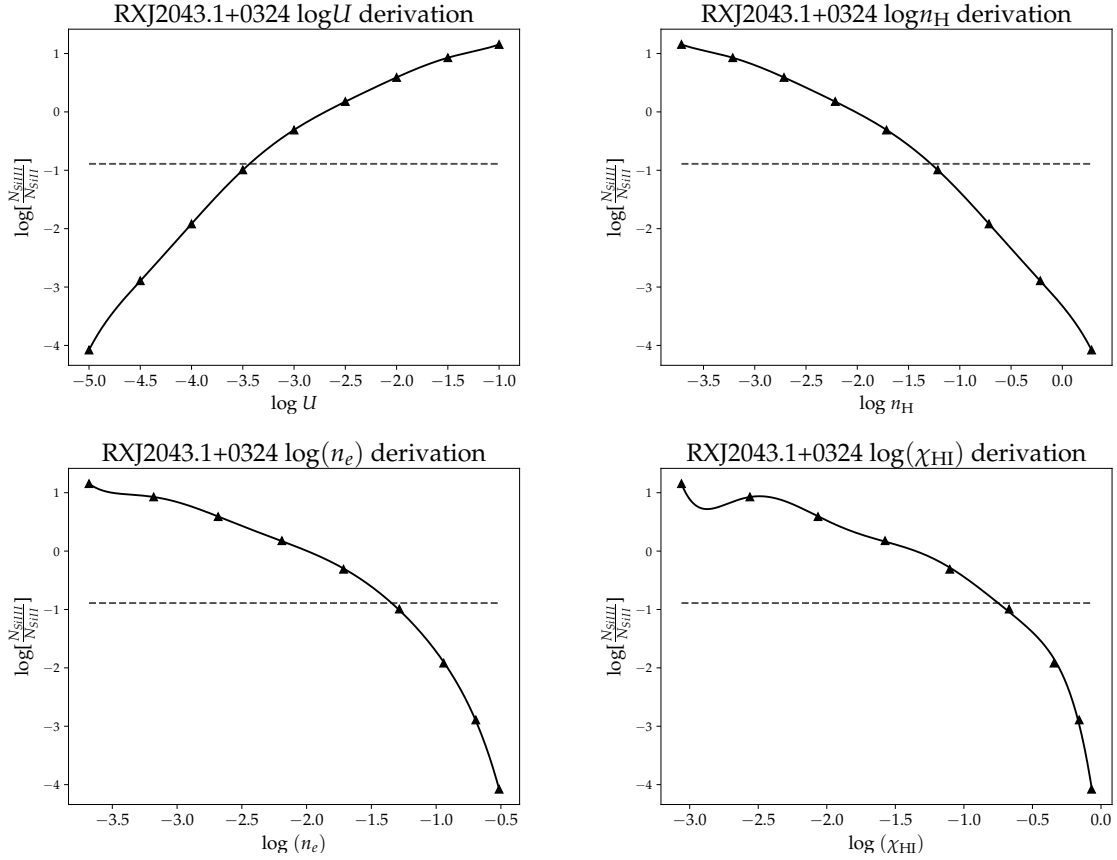
Figure A.6: Above, we plot the derivation of the following physical properties for sightline E: (top left) ionization parameter, (top right) total hydrogen number density in cm^{-3}, (bottom left) electron density in cm^{-3}, and (bottom right) neutral hydrogen fraction. They are matched to $\log(N_{\text{Si III}}/N_{\text{Si II}}) > -0.99$. All values are plotted in log space.
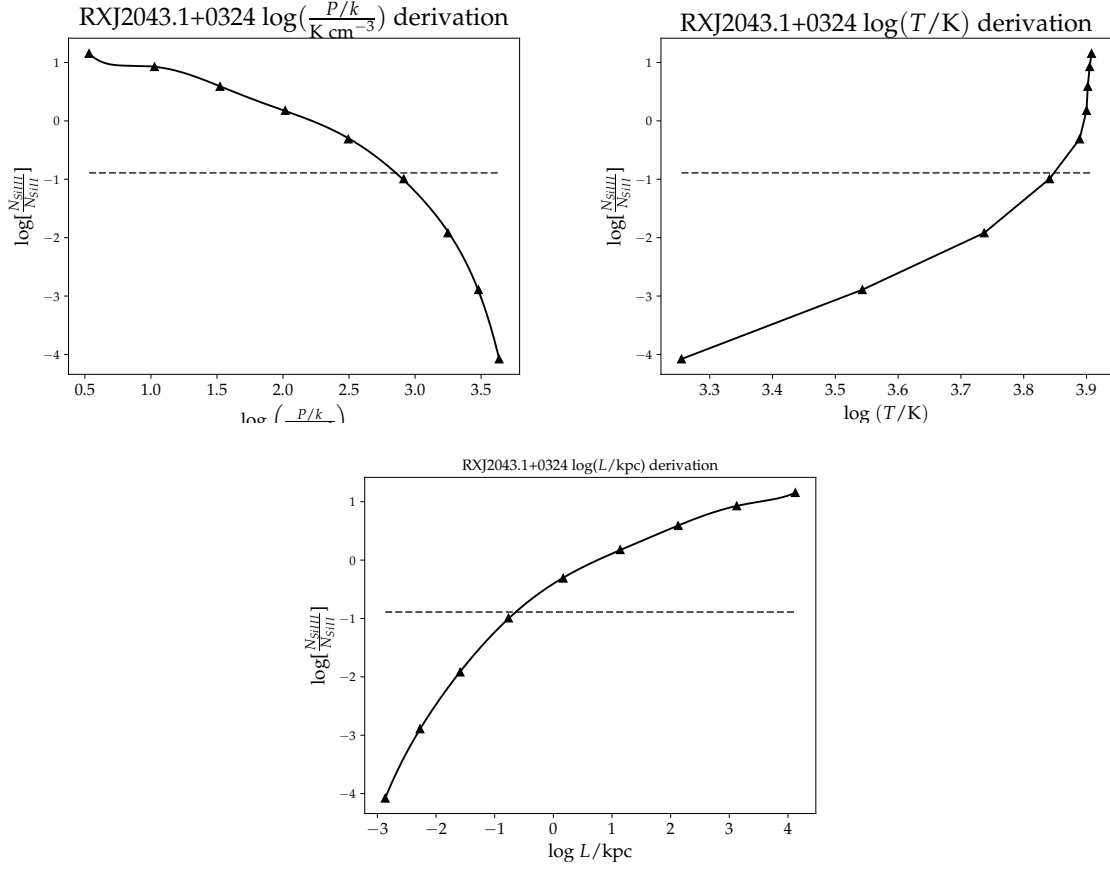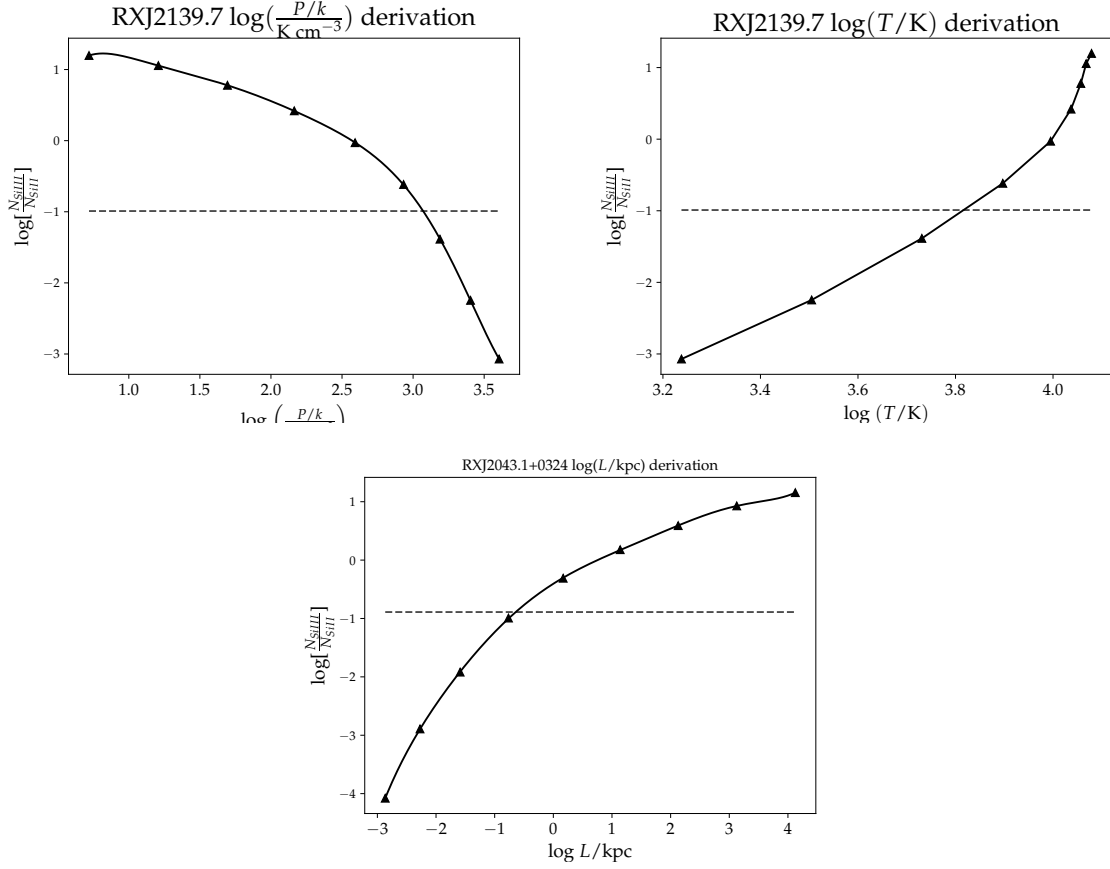
Figure A.7: Above, we plot the derivation of the following physical properties for sight-line C: (top left) pressure divided by the Boltzmann constant in K cm^{-3}, (top right) temperature in K, and (bottom) line-of-sight length in kpc. They are matched to $\log(N_{\text{Si III}}/N_{\text{Si II}}) > -0.99$. All values are plotted in log space.
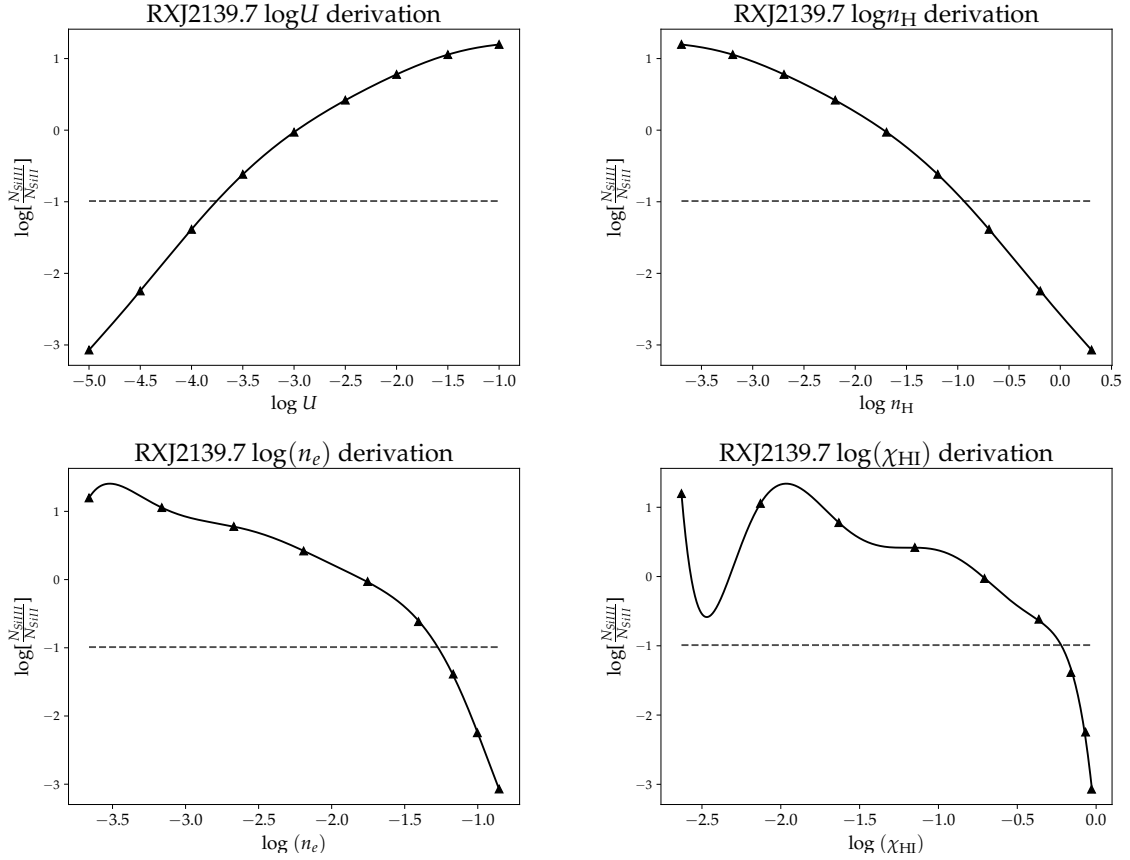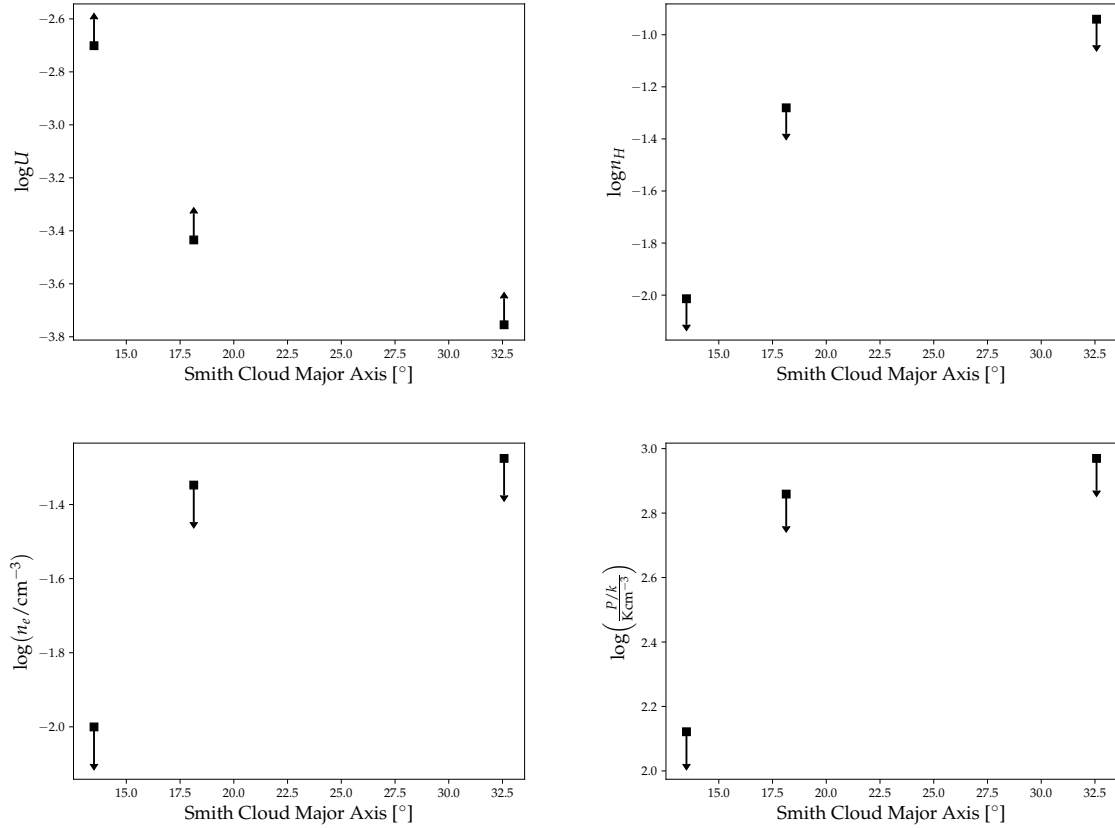
Figure A.8: The following physical properties are plotted as a function of Smith Cloud major axis coordinate: (top left) ionization parameter, (top right) total hydrogen number density in cm^{-3}, (bottom left) electron density in cm^{-3}, and (bottom right) pressure per Boltzmann constant in K cm^{-3}. Up arrows mean a lower limit, and down arrows mean an upper limit. From left to right, these points represent sightlines A, C, and E.
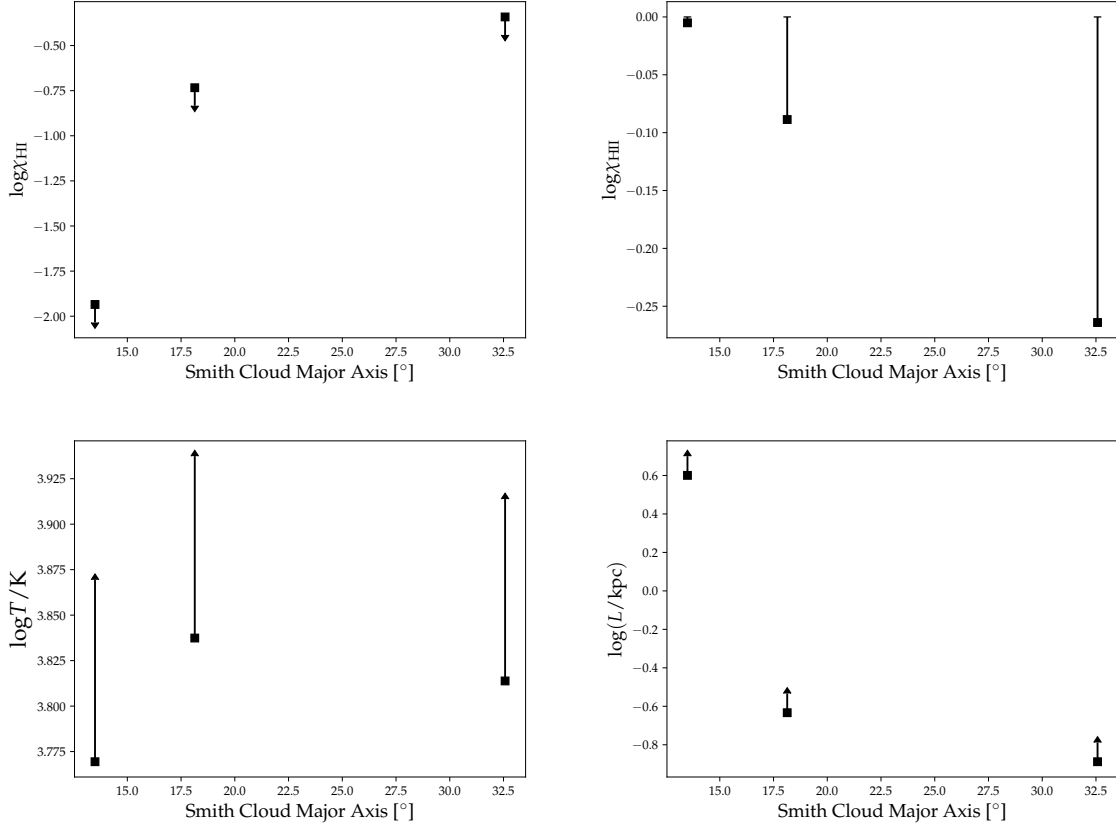
Figure A.9: The following physical properties are plotted as a function of Smith Cloud major axis coordinate: (top left) neutral hydrogen fraction, (top right) ionized hydrogen fraction, (bottom left) temperature in K, and (bottom right) line-of-sight length of the cloud in kpc. Up arrows mean a lower limit, and down arrows mean an upper limit. $\log \chi_{\mathrm{H\,II}}$ has a hard upper limit at 0.00, since this signifies 100% of the gas being ionized. From left to right, these points represent sightlines A, C, and E.

Appendix B

Additional Voigt-fitted Lines for

Sightlines A & B

Since we have provide analysis for two new QSO sightlines, in this appendix, we provide additional line-fitting parameters for these two sightlines.

Ion/Wavelength	N_X (atoms cm^{-2})	$v_{\mathrm{SC,LSR}}$ (km s^{-1})	b_{SC} (km s^{-1})
H I λ21cm (1)^d	19.21 ± 0.03	$+41.07 \pm 0.64$	12.43 ± 0.11
H I λ21cm (2)^d	18.67 ± 0.06	$+46.78 \pm 0.32$	3.44 ± 0.171
H I λ21cm (3)^d	< 18.18	$\approx +133$	≈ 27
S IIλ1259	14.41 ± 0.10	$+123.9\pm8.4$	25.0^a
Si IIλ1190, 1193, 1260, 1304	13.92 ± 0.04	$+104.7 \pm 3.5$	37.6 ± 3.1
Si IIIλ1206	$> 13.85^c$	104^a	40.00^a
Si IV λ1393, 1402	13.28 ± 0.08	$+116.1 \pm 9.8$	35.0^a
O I λ1302	14.63 ± 0.01	$+112.4 \pm 7.0$	35.0^a

Table B.1: A table of column densities, center velocities, and Doppler parameter values for various ions and transitions along Sightline A.

^{a} These values were anchored in the VoigtFit software in order to find the optimal fit that had a reasonable Milky Way and Smith Cloud component.
^{c} This value is a lower bound on the column density based on the AOD method.
^{d} We fit two Gaussian components to the intermediate-velocity component of the Smith Cloud. However, the H I emission that best-matches with the UV is numerically integrated but lies below the 3σ detection limit, which is reported in the column for H I λ21cm (3)

Ion/Wavelength	$\log_{10}(N_X/\mathrm{cm}^{-2})$	$v_{\mathrm{SC,LSR}}$ (km s^{-1})	b_{SC}(km s^{-1})
H I λ21 cm (1)^d	19.14 ± 0.04	$+58.4 \pm 0.3$	8.3 ± 0.2
H I λ21 cm (2)^d	19.30 ± 0.04	$+69.1 \pm 1.0$	16.7 ± 0.6
S II λ1250, 1253, 1259	15.00 ± 0.16	$+68.3 \pm 9.0$	18.2 ± 11.9
Si II λ1190, 1193, 1260, 1304	$> 13.93^c$	72.5^a	25.00^a
Si III λ1206	$> 13.49^c$	72.2^a	25.00^a
Si IV λ1393, 1402	12.90 ± 0.39	80.9^a	36.0 ± 36.7
C II $^*\lambda$1335	14.01 ± 0.05	72.5 ± 2.7	25.2 ± 4.2
O I λ1302	14.69 ± 0.17	72.5^a	30.5 ± 10.6

Table B.2: A table of column densities, center velocities, and Doppler parameter values for various ions and transitions along Sightline B.

^{a} These values were anchored in the VoigtFit software in order to find the optimal fit that had a reasonable Milky Way and Smith Cloud component.
^{c} This value is a lower bound on the column density based on the AOD method.
^{d} For this sightline, we have two kinematic components of H I.

Bibliography

Armillotta, L., Fraternali, F., Werk, J. K., Prochaska, J. X., & Marinacci, F. 2017, Monthly Notices of the Royal Astronomical Society, 470, 114

Asplund, M., Grevesse, N., Sauval, A. J., & Scott, P. 2009, The Annual Review of Astronomy and Astrophysics, 47, 481

Barger, K. A., Nidever, D. L., Huey-You, C., Lehner, N., Rueff, K., Freeman, P., Birdwell, A., Wakker, B. P., Bland-Hawthorn, J., Benjamin, R., & Ciampa, D. A. 2020, The Astrophysical Journal, 902, 154

Bland-Hawthorn, J. & Maloney, P. R. 1999, in ASP Conf. Ser., Vol. 166, Stromlo Workshop on High-Velocity Clouds, ed. B. K. Gibson & M. E. Putman, 212–+

Bland-Hawthorn, J. & Maloney, P. R. 2001, The Astrophysical Journal Letters, 550, L231

Choi, J.-H. & Nagamine, K. 2009, Monthly Notices of the Royal Astronomical Society, 393, 1595

Cohen, E. R., Lide, D. R., & Trigg, G. L. 2003, AIP physics desk reference

Dickey, J. M. & Lockman, F. J. 1990, The Annual Review of Astronomy and Astrophysics, 28, 215

Draine, B. T. 2011, Physics of the Interstellar and Intergalactic Medium

Ferland, G. J., Chatzikos, M., Guzmán, F., Lykins, M. L., van Hoof, P. A. M., Williams, R. J. R., Abel, N. P., Badnell, N. R., Keenan, F. P., Porter, R. L., & Stancil, P. C. 2017, , 53, 385

Fox, A., James, B., Roman-Duval, J., Rafelski, M., & Sonnentrucker, P. 2018a, The Spectral Resolution of the COS FUV channel at Lifetime Position 4, Instrument Science Report COS 2018-7, 25 pages

Fox, A. J., Barger, K. A., Wakker, B. P., Richter, P., Antwi-Danso, J., Casetti-Dinescu, D. I., Howk, J. C., Lehner, N., D'Onghia, E., Crowther, P. A., & Lockman, F. J. 2018b, The Astrophysical Journal, 854, 142

Fox, A. J., Lehner, N., Lockman, F. J., Wakker, B. P., Hill, A. S., Heitsch, F., Stark, D. V., Barger, K. A., Sembach, K. R., & Rahman, M. 2016, The Astrophysical Journal Letters, 816, L11

Fox, A. J., Richter, P., Ashley, T., Heckman, T. M., Lehner, N., Werk, J. K., Bordoloi, R., & Peeples, M. S. 2019, The Astrophysical Journal, 884, 53

Francis, C. & Anderson, E. 2009, , 14, 615

—. 2014, Celestial Mechanics and Dynamical Astronomy, 118, 399

Henley, D. B., Gritton, J. A., & Shelton, R. L. 2017, The Astrophysical Journal, 837, 82

Hill, A. S., Haffner, L. M., & Reynolds, R. J. 2009, The Astrophysical Journal, 703, 1832

Hill, A. S., Mao, S. A., Benjamin, R. A., Lockman, F. J., & McClure-Griffiths, N. M. 2013, The Astrophysical Journal, 777, 55

Jenkins, E. B. 2009, The Astrophysical Journal, 700, 1299

Kalberla, P. M. W., Burton, W. B., Hartmann, D., Arnal, E. M., Bajaja, E., Morras, R., & Pöppel, W. G. L. 2005, Astronomy and Astrophysics, 440, 775

Kalberla, P. M. W. & Kerp, J. 2009, The Annual Review of Astronomy and Astrophysics, 47, 27

Kalberla, P. M. W., McClure-Griffiths, N. M., Pisano, D. J., Calabretta, M. R., Ford, H. A., Lockman, F. J., Staveley-Smith, L., Kerp, J., Winkel, B., Murphy, T., & Newton-McGee, K. 2010, Astronomy and Astrophysics, 521, A17

Kennicutt, R. C. & Evans, N. J. 2012, The Annual Review of Astronomy and Astrophysics, 50, 531

Kerp, J., Burton, W. B., Egger, R., Freyberg, M. J., Hartmann, D., Kalberla, P. M. W., Mebold, U., & Pietz, J. 1999, Astronomy and Astrophysics, 342, 213

Khaire, V. & Srianand, R. 2019, Monthly Notices of the Royal Astronomical Society, 484, 4174

Krogager, J.-K. 2018, VoigtFit: A Python package for Voigt profile fitting

Lépine, J. R. D., Sartori, M. J., & Marinho, E. P. 1999, in Astronomical Society of the Pacific Conference Series, Vol. 166, Stromlo Workshop on High-Velocity Clouds, ed. B. K. Gibson & M. E. Putman, 165

Lockman, F. J., Benjamin, R. A., Heroux, A. J., & Langston, G. I. 2008, The Astrophysical Journal Letters, 679, L21

Madau, P. 2002, in Encyclopedia of Astronomy and Astrophysics, ed. P. Murdin, E1821

Marasco, A. & Fraternali, F. 2016, arXiv e-prints, arXiv:1609.06309

McClure-Griffiths, N. M., Pisano, D. J., Calabretta, M. R., Ford, H. A., Lockman, F. J., Staveley-Smith, L., Kalberla, P. M. W., Bailin, J., Dedes, L., Janowiecki, S., Gibson, B. K., Murphy, T., Nakanishi, H., & Newton-McGee, K. 2009, Astrophysical Journal Supplement, 181, 398

Meeks, M. L. 1976, Methods of experimental physics. Vol. 12. Astrophysics. Part C: Radio observations.

Putman, M. E., Peek, J. E. G., & Joung, M. R. 2012, The Annual Review of Astronomy and Astrophysics, 50, 491

Robitaille, T. P. & Whitney, B. A. 2010, The Astrophysical Journal Letters, 710, L11

Savage, B. D. & Sembach, K. R. 1991, The Astrophysical Journal, 379, 245

Schinnerer, E., Meidt, S. E., Pety, J., Hughes, A., Colombo, D., García-Burillo, S., Schuster, K. F., Dumas, G., Dobbs, C. L., Leroy, A. K., Kramer, C., Thompson, T. A., & Regan, M. W. 2013, The Astrophysical Journal, 779, 42

Shu, F. H. & Adams, F. C. 1987, in Circumstellar Matter, ed. I. Appenzeller & C. Jordan, Vol. 122, 7

Smith, G. P. 1963, , 17, 203

Smith, L. F., Biermann, P., & Mezger, P. G. 1978, Astronomy and Astrophysics, 66, 65

Sobral, D., Smail, I., Best, P. N., Geach, J. E., Matsuda, Y., Stott, J. P., Cirasuolo, M., & Kurk, J. 2013, Monthly Notices of the Royal Astronomical Society, 428, 1128

Taylor, J. R. 1997, Introduction to Error Analysis, 2nd Ed. (cloth)

Tepper-García, T. & Bland-Hawthorn, J. 2018, Monthly Notices of the Royal Astronomical Society, 473, 5514

Wolfe, S. A., Lockman, F. J., & Pisano, D. J. 2016, The Astrophysical Journal, 816, 81

VITA

Personal Background	Johanna Tamatha Vazquez
	Elon, VA
	Daughter of Tamatha and Jaime Vazquez
Education	Diploma, Homeschool,
	Elon, VA, 2017
	Associate of Arts & Sciences, Central Virginia Community College,
	Lynchburg, VA, 2017
	Baccalaureate of Science, Physics, Randolph College,
	Lynchburg, VA, 2020
Experience	Summer research assistant, Cornell University, Ithaca, NY,
	2018
	Summer research assistant, Randolph College, Lynchburg, VA,
	2019
	Teaching assistantship, Texas Christian University, Fort
	Worth, 2020-2022
	Research assistantship, Texas Christian University, Fort
	Worth, 2021
Professional Memberships	American Astronomical Society, Sigma Pi Sigma

ABSTRACT

THE SMITH CLOUD: A CASE STUDY OF THE DYNAMIC DISRUPTION OF A
HIGH-VELOCITY GAS CLOUD ON APPROACH TO THE MILKY WAY GALAXY

by Johanna T. Vazquez, 2022
Department of Physics and Astronomy
Texas Christian University

Kathleen A. Barger, Associate Professor of Physics

L_* galaxies are on a trend of decreasing stellar and planetary formation. To continue their current rates of star-formation, galaxies must find outside sources of gas and dust to accrete onto their disks. However, the accretion of extragalactic gas is not straightforward. This gas must surpass a Galactic halo of $T \sim 10^6$ K as well as the incident radiation from the Galaxy itself. The effect of these processes on the survival of infalling gas clouds is not well-understood. To illuminate our understanding of these processes, we study the physical properties of the Smith Cloud, a high-velocity cloud (HVC) in the Milky Way Galaxy's halo using the Hubble Space Telescope and photoionization simulations. After studying two quasar sightlines along an adjacent fragment of the Smith Cloud and three quasar sightlines along the tail, we find that the metallicity seems to decrease the further downstream a sightline is from the main body of the Smith Cloud and that the gas is at least 46.5% ionized. These results can help improve our understanding on the origins of the Smith Cloud and how it may be mixing with the Milky Way's Galactic halo.